REVIEW　　　　　　　　　　　　　　　　　　　　　**Open Access**

Optical interactions in plasmonic nanostructures

Wounjhang Park

Abstract

We present a review of plasmonic nanostructures in which the constituent materials are coupled together by optical interactions. The review first provides a comprehensive coverage of theoretical framework where the optical interactions are described by the multiple scattering among the nanostructures. We then discuss the two limiting cases of weak and strong interactions. The weak interaction regime is described well by the effective medium theory while the strong interaction regime requires theoretical tools that can describe the new eigenmodes delocalized over the entire system. Weakly interacting plasmonic nanostructures have been studied extensively in the metamaterials research, which has been a major research thrust in photonics during the past decade. This review covers some of the latest examples exhibiting perfect absorption and invisibility. Strongly coupled systems started to receive attention recently. As a representative example, plasmonic molecules exhibiting Fano resonance are discussed in detail. Plasmonic nanostructures offer an excellent platform to engineer nanoscale optical fields. With the recent progress in nanofabrication technologies, plasmonic nanostructures offer a highly promising pathway to discovering new phenomena and developing novel optical devices.

1 Introduction

In the Drude theory, metal is modeled as a system of free electron gas undergoing forced oscillation with some damping. Other than some notable exceptions such as the strong interband absorption involving the d band in transition metals, the Drude model generally provides good descriptions of the optical properties of metals. It predicts that in the low frequency region the induced polarization oscillates 180° out-of-phase with the external field, resulting in negative permittivity and consequently high reflectivity. At certain frequencies, the electron gas can also undergo collective oscillations whose quantum is called plasmon. The collective oscillation may involve volume charge density (volume plasmon) or surface charge density (surface plasmon). Volume plasmons are longitudinal oscillations and cannot be excited by electromagnetic waves which are normally transverse. Surface plasmons, however, interact strongly with light. By storing a significant portion of its energy in oscillating electron gas, surface plasmon offers an effective means to localize light down to length scales much smaller than wavelength. For this reason, the past decades have seen an explosive growth in research on surface plasmon nanophotonics.

One of the topics of high interest is nanoscale waveguiding with potential applications in integrated photonics for which a large body of literature exists [1]. Another important class of plasmonic nanostructures more relevant to this review are those supporting localized surface plasmon (LSP) modes. These structures include metal nanoparticles of various shapes, nanoholes in metal films, and some variations of these. The LSP resonances typically manifest themselves with strong scattering and absorption. The characteristic color arising from the LSP resonances has enabled a wide range of applications from the medieval stained glasses to modern optical sensors. For example, colorimetric sensing of biomolecules and ions has been demonstrated [2,3]. Also, strongly scattering nanoparticles have been used to enhance contrast in dark-field microscopy and optical coherence tomography [4] while thermal ablasing strongly absorbing nanoparticles is being actively developed for targeted therapies of various diseases [5,6].

LSP naturally provides a highly localized and intense optical field which consequently enhances a variety of optical processes. The best-known example is surface enhanced Raman scattering (SERS). Using a rough silver surface, Raman scattering by a single molecule has been observed with enhancements up to a factor of 10^{14} [7]. Much of the enhancement is believed to arise from the local field enhancement due to the highly localized hot spots produced by the silver nanostructure

Correspondence: won.park@colorado.edu
Department of Electrical, Computer & Energy Engineering,
University of Colorado, Boulder, CO 80309-0425, USA

[8]. Surface plasmon resonance can also be used to enhance luminescence [9] and Förster energy transfer process [10,11]. Since the optical processes depend on the local field strength, strong emphasis has been placed on achieving higher local field enhancement using novel nanostructure geometries. These structures are generally termed nano-antennas analogous to conventional antennas in the microwave frequency region and have been the subject of extensive research in the past decade [12]. Since hot spots are typically formed in the nano-gap between plasmonic nanoparticles, the nano-antenna research naturally directed attention to the interaction between LSP modes, which is the main subject of this review. An important recent development in this field is the concept of plasmon hybridization [13]. In this picture, the individual LSP modes in closely spaced nanoparticles hybridize to form a set of new modes delocalized over the entire structure, in much the same way atomic orbitals hybridize to form molecular orbitals in real molecules. For this reason, these plasmonic nanostructures are also called plasmonic molecules. The hybridized modes in plasmonic molecules have been extensively studied. The simplest form of plasmonic molecule is a dimer or a pair of nanoparticles in which the plasmon resonance of single nanoparticle hybridizes to produce symmetric and anti-symmetric dimer plasmons [14]. Hybridization in more complex structures has also been studied, e.g. trimer [15], quadrumer [16], hexamer [17] and most widely heptamer [18-22]. In these complex structures, symmetry properties of the hybridized plasmon modes should be described by the group representation theory [23]. In this formalism, how each plasmon mode transforms under the symmetry operations is described by the irreducible representations of the symmetry group. This allows for a systematic description of modes with complex field profiles and also their interaction with incident optical fields, providing a complete picture when combined with the numerical techniques that can precisely calculate the hybridized LSP modes. It is noted that the group theoretical approach classifying the symmetry properties of plasmon modes does not require any approximations. For example, in nanostructures with features sizes much smaller than the wavelength, the plasmon modes exhibit predominantly electric dipole nature and are often approximated as point dipoles. The group theoretical approach, however, does not require dipole approximation and is equally applicable to larger and more complex structures exhibiting higher order mulitpole components.

The strength and nature of the optical interaction between plasmonic nanostructures varies with the distance. For long distances, the interaction is mainly radiative and involves propagating electromagnetic waves undergoing multiple scattering among the plasmonic nanostructures. In this case, the original character of the individual LSP modes should largely be preserved. For short distances, evanescently decaying near-field components should be taken into account. In principle, the near-field interaction can be treated the same way as the far-field interaction in the general framework of multiple scattering theory. That is, the evanescent modes undergo multiple scattering between nanostructures as well as the propagating modes. In extreme short distances, where the individual LSP modes have significant overlaps with one another, the near-field interaction will dominate and hybridization resulting in fully delocalized modes would occur. This review is aimed at providing a unified view of plasmonic nanostructures in which the strength of the interaction among individual metallic components is varied. We will first present a theoretical framework followed by examples of nanostructures and their optical properties in the weak and strong coupling regimes.

2 Review
2.1 Theoretical framework
2.1.1 Classical description of surface plasmon resonance
Surface plasmon, while inherently a quantum mechanical entity, is generally well described by the classical theory where surface plasmon presents itself as a surface resonance. There are of course quantum mechanical characteristics that cannot be fully described by the classical theory such as nonlocal response of electrons [24,25], tunneling and screening effect [26], spontaneous and stimulated emission of photons [27] and plasmons [28,29], to name a few. Nevertheless, the classical theory has proved sufficient for a wide range of systems. The classical theory is based on the Maxwell's equations where the boundary conditions are set up by the material properties specified by the macroscopic permittivity and permeability. For the planar geometry, surface wave solutions with fields decaying exponentially away from the interfaces can be found. In the simplest example of a single planar interface between semi-infinite metal and dielectric, the surface wave vector, q, is given by the dispersion relation [30],

$$q = \frac{\omega}{c}\sqrt{\frac{\varepsilon_1 \varepsilon_2}{\varepsilon_1 + \varepsilon_2}} \tag{1}$$

where ε_1 and ε_2 are the permittivities of metal and dielectric medium, respectively, and often Drude model is used for the metal permittivity, $\varepsilon_1(\omega) = 1 + \omega_p^2/(\omega^2 + i\gamma\omega)$ where ω_p is the plasma frequency and γ is the damping parameter. This surface wave solution specifies the optical mode often called surface plasmon-polariton (SPP). For the lossless case where the permittivities are purely real, the dispersion relation has a singularity when $\varepsilon_1 + \varepsilon_2 = 0$. This condition defines the surface plasmon frequency, ω_s, which is given by $\omega_s = \omega_p/\sqrt{1 + \varepsilon_2}$, when using the Drude model for metal permittivity. Here ω_p is the plasma frequency of the electron gas. When there is finite loss, the metal permittivity is complex and the resonance condition should be

written as which defines the condition for maximum electric field amplitude. This theory can be straightforwardly extended to more complex geometries involving multiple interfaces to obtain SPP solutions [31-34]. The localized surface plasmon modes (LSPs) generally require numerical calculations as the surface plasmon modes are highly sensitive to the details of the given geometry. An important exception is the highly symmetric geometry of sphere and circular cylinder for which a complete analytical solution can be obtained by using the Mie theory where the scattering and absorption cross-sections are given by the scattering coefficients a_n and b_n corresponding to various multipole terms [35]. For small spheres, the scattering coefficients a_n have vanishing denominators when $m^2 = -(n+1)/n$, where m is the relative refractive index of sphere relative to the embedded medium and n is an integer. This leads to a sharp increase in both scattering and absorption. In the limit of extremely small sphere, the extinction is dominated by the leading term, a_1, resulting in the resonance condition, $m^2 = -2$ or $\varepsilon_1 = -2\varepsilon_2$ when using the Drude model for the metal permittivity. For the lossless case where the permittivities are purely real, the resonance condition is satisfied when $\omega = \omega_p/\sqrt{2+\varepsilon_2}$, which is sometimes called the Fröhlich frequency. Thus, the LSPs supported by metallic spheres and cylinders may be considered special cases of Mie resonances.

2.1.2 Multiple scattering theory

We now consider a cluster of nanoparticles or nanostructures which individually support LSP resonances. The key additional consideration needed to properly describe the cluster is the multiple scattering between the individual components. Since analytical solutions are available for spheres, it is instructive to consider a cluster of nanospheres. In this case, the scattering by the individual spheres can be described by the standard Mie theory. The fundamental difference from the single sphere case is that for each sphere in the cluster the incident field is the combination of the actual incident field impinging on the cluster and the scattered fields by all other spheres in the cluster [36-38]. To briefly provide an overview of this process, we first remind the reader of the standard Mie theory for a single sphere where all fields are described in the coordinate system with the sphere located at the origin. The incident and scattered fields are then expressed in terms of the vector spherical harmonics,

$$\mathbf{E}_{scat} = \sum_{n=1}^{\infty}\sum_{m=-n}^{n} iE_{mn}\left(a_{mn}\mathbf{N}_{mn}^{(3)} + b_{mn}\mathbf{M}_{mn}^{(3)}\right)$$

$$\mathbf{E}_{int} = \sum_{n=1}^{\infty}\sum_{m=-n}^{n} iE_{mn}\left(d_{mn}\mathbf{N}_{mn}^{(1)} + c_{mn}\mathbf{M}_{mn}^{(1)}\right) \quad (2)$$

$$\mathbf{E}_{inc} = \sum_{n=1}^{\infty}\sum_{m=-n}^{n} iE_{mn}\left(p_{mn}\mathbf{N}_{mn}^{(1)} + q_{mn}\mathbf{M}_{mn}^{(1)}\right)$$

where $\mathbf{E}_{scat}$, $\mathbf{E}_{int}$ and $\mathbf{E}_{inc}$ represent scattered, internal and incident fields, respectively, $\mathbf{M}_{mn}$ and $\mathbf{N}_{mn}$ are the vector spherical harmonics. Similar expressions for the magnetic fields are readily obtained from the Maxwell's equations. The coefficients p_{mn} and q_{mn} are naturally dependent on the exact form of the incident field. For plane wave incidence, all terms with $m \neq 1$ vanish and the full expressions for the coefficients, a_n, b_n, c_n, d_n, p_n and q_n are available in the literature [39]. To describe multiple scattering in a cluster made of L spheres, the coefficients, p_{mn} and q_{mn}, describing the incident field for a sphere needs to be rewritten to include the scattered fields by all other spheres. This in turn requires translating all vector harmonics functions separately obtained in the coordinate systems of individual spheres into the common coordinate system so they may be added. This is achieved by the addition theorem of vector spherical harmonics:

$$\mathbf{M}_{mn} = \sum_{v=0}^{\infty}\sum_{\mu=-v}^{v}\left(A0_{\mu v}^{mn}\mathbf{M}_{mn}' + B0_{\mu v}^{mn}\mathbf{N}_{mn}'\right)$$

$$\mathbf{N}_{mn} = \sum_{v=0}^{\infty}\sum_{\mu=-v}^{v}\left(B0_{\mu v}^{mn}\mathbf{M}_{mn}' + A0_{\mu v}^{mn}\mathbf{N}_{mn}'\right) \quad (3)$$

where $\mathbf{M}_{mn}$ and $\mathbf{N}_{mn}$ are the vector spherical harmonics about origin O, $\mathbf{M}_{mn}'$ and $\mathbf{N}_{mn}'$ are the vector spherical harmonics about origin O′, and $A0_{\mu v}^{mn}$ and are the additional coefficients whose complete expressions are available in the literature [36]. One can then express the scattered field by the lth sphere in the coordinate system of jth sphere using the new coefficients, p_{mn}^{lj} and q_{mn}^{lj},

$$p_{mn}^{lj} = -\sum_{v=0}^{\infty}\sum_{\mu=-v}^{v}\left(a_{\mu v}^{l}A_{mn}^{\mu v}(l,j) + b_{\mu v}^{l}B_{mn}^{\mu v}(l,j)\right)$$

$$q_{mn}^{lj} = -\sum_{v=0}^{\infty}\sum_{\mu=-v}^{v}\left(a_{\mu v}^{l}B_{mn}^{\mu v}(l,j) + b_{\mu v}^{l}A_{mn}^{\mu v}(l,j)\right) \quad (4)$$

where $A_{\mu v}^{mn}$ and $B_{\mu v}^{mn}$ are related to $A0_{\mu v}^{mn}$ and $B0_{\mu v}^{mn}$ as given in Ref. [36]. Imposing the boundary conditions at the surfaces of the spheres finally leads to a set of linear equations

$$a_{mn}^{j} = a_n^{j}\left\{p_{mn}^{jj} - \sum_{l\neq j}\sum_{v=0}^{\infty}\sum_{\mu=-v}^{v}\left(a_{\mu v}^{l}A_{mn}^{\mu v}(l,j) + b_{\mu v}^{l}B_{mn}^{\mu v}(l,j)\right)\right\}$$

$$b_{mn}^{j} = b_n^{j}\left\{q_{mn}^{jj} - \sum_{l\neq j}\sum_{v=0}^{\infty}\sum_{\mu=-v}^{v}\left(a_{\mu v}^{l}B_{mn}^{\mu v}(l,j) + b_{\mu v}^{l}A_{mn}^{\mu v}(l,j)\right)\right\}$$

$$(5)$$

Once the scattering coefficients, and, are found from the above equations, then the total scattered field by the entire cluster can be obtained by using the addition

theorem one more time to express all fields in the common coordinate system of j_0th sphere,

$$\mathbf{E}_{scat} = \sum_{n=1}^{\infty} \sum_{m=-n}^{n} iE_{mn}\left(a_{mn}\mathbf{N}_{mn}^{(3)} + b_{mn}\mathbf{M}_{mn}^{(3)}\right) \qquad (6)$$

where

$$a_{mn} = \sum_{l=1}^{L}\sum_{v=0}^{\infty}\sum_{\mu=-v}^{v}\left(a_{\mu v}^{l}A_{mn}^{\mu v}(l,j_0) + b_{\mu v}^{l}B_{mn}^{\mu v}(l,j_0)\right)$$

$$b_{mn} = \sum_{l=1}^{L}\sum_{v=0}^{\infty}\sum_{\mu=-v}^{v}\left(a_{\mu v}^{l}B_{mn}^{\mu v}(l,j_0) + b_{\mu v}^{l}A_{mn}^{\mu v}(l,j_0)\right)$$

$$(7)$$

The scattering cross section can be written in a similar fashion to the single sphere Mie scattering case,

$$C_{scat} = \frac{4\pi}{k^2}\sum_{n=0}^{\infty}\sum_{m=-n}^{n} n(n+1)(2n+1)\frac{(n-m)!}{(n+m)!}\left(|a_{mn}|^2 + |b_{mn}|^2\right)$$

$$(8)$$

A similar multiple scattering theory has also been developed for an infinitely periodic array of spheres [40-42]. In this case, since the system has infinite extent, the main concern is the propagation of light inside the periodic array. Due to the similarity to the Kohn-Korringa-Rostocker (KKR) method widely used for electronic energy band structure studies, this technique is sometimes called the vector KKR method. Once again, vector spherical harmonics are used to take advantage of the spherical geometry. Following the original development by Stefanou et al. [40,43], we begin with the general expression for spherical wave expansion given in equation (6) for a two-dimensional (2D) periodic array of spheres. When a plane wave is incident on the 2D array, the scattered wave must be expressed as a sum of the waves scattered by all spheres in the 2D plane. Due to the periodicity, the wave scattered by a sphere at $\mathbf{r} = \mathbf{R}_n$ differs only by a simple phase factor, $\exp(i\mathbf{k}_{||} \cdot \mathbf{R}_n)$, from the wave scattered by a sphere at the origin. Here, $\mathbf{k}_{||}$ represents the tangential component of k-vector parallel to the plane of spheres. The scattered field can then be written as,

$$E_{scat} = \sum_{n=1}^{\infty}\sum_{m=-n}^{n}\left(\frac{i}{k}b_{mn}^{E}\nabla \times \sum_{\mathbf{R}_n}\exp(i\mathbf{k}_{||}\cdot\mathbf{R}_n)h_n(kr_n)\mathbf{X}_{mn}(\theta,\phi)\right.$$
$$\left. + b_{mn}^{H}\sum_{\mathbf{R}_n}\exp(i\mathbf{k}_{||}\cdot\mathbf{R}_n)h_n(kr_n)\mathbf{X}_{mn}(\theta,\phi)\right)$$

$$(9)$$

where b_{mn} are coefficients to be determined, $\mathbf{r}_n = \mathbf{r} - \mathbf{R}_n$, h_n is the spherical Hankel function and $\mathbf{X}_{mn}$ is defined as $\sqrt{n(n+1)}\mathbf{X}_{mn} = -i\mathbf{r} \times \nabla Y_{mn}$ where Y_{mn} is the spherical harmonics function. While we try to keep the notation of original authors as much as possible, we note that the above equation is essentially in the same form as equation

(6) where b_{mn}^{E} and b_{mn}^{H} in equation (9) are analogous to a_{mn} and b_{mn} coefficients in equation (6). The phase factor, $\exp(i\mathbf{k}_{||} \cdot \mathbf{R}_n)$, in the above equation allows us to express the scattered field in terms of plane waves with wave vectors,

$$K_g^{\pm} = \left(\mathbf{k}_{||} + \mathbf{g}, \pm\sqrt{k^2 - (\mathbf{k}_{||} + \mathbf{g})^2}\right) \qquad (10)$$

Here $\mathbf{k}_{||}$ represents the reduced wave vector defined as $\mathbf{k}_{tangential} = \mathbf{k}_{||} + \mathbf{g}$, where $\mathbf{g}$ is the reciprocal lattice vectors of the 2D lattice, so that $\mathbf{k}_{||}$ now represents a vector within the unit cell of the 2D reciprocal lattice or the surface Brillouin zone. The sign in the superscript indicates forward and backward propagating waves in the direction perpendicular to the 2D plane. Now we construct the same plane wave expansion for the incident wave as well and obtain a matrix equation relating the coefficients of the incident wave and the total scattered wave,

$$[E_{scat}]_{g,i}^{s} \equiv \sum_{g',i'} M_{gi,g'i'}^{ss'}[E_{inc}]_{g',i'}^{s'} \qquad (11)$$

where the new subscripts i, i' indicate the Cartesian components. The explicit expression for the matrix $\mathbf{M}'$ may be found in Ref. [44]. Equation (11) fully describes the interaction of a 2D periodic array of spheres with an incident light but, since the summation is infinite, actual numerical evaluations will involve truncation which introduces numerical errors. Now we extend the theory to three-dimensional (3D) array composed of multiple layers of 2D arrays by constructing a transfer matrix describing the multiple scattering effects between the adjacent 2D planes. That is, the field between the nth and $(n + 1)$th layers are determined by the scattering by the two neighboring planes of spheres. More specifically, the backward propagating wave in the region between nth and $(n + 1)$th layer is the sum of the forward propagating wave in the same region back-scattered by $(n + 1)$th layer and the backward propagating wave between the $(n + 1)$th and $(n + 2)$th layers transmitted (or forward-scattered) by the $(n + 1)$th layer. The forward propagating wave is similarly defined. The transmission and reflection matrices are obtained from the matrix $\mathbf{M}$ in equation (11) modified to account for the shift of origin between the two adjacent planes. This way, one obtains equations relating fields at adjacent layers which must also satisfy the Bloch theorem because the system is periodic in the 3rd dimension as well. Combining the multiple scattering equations and the Bloch theorem, one obtains an eigenvalue equation,

$$\begin{pmatrix} \mathbf{Q}^{++} & \mathbf{Q}^{+-} \\ -[\mathbf{Q}^{--}]^{-1}\mathbf{Q}^{-+}\mathbf{Q}^{++} & [\mathbf{Q}^{--}]^{-1}[\mathbf{Q}^{-+}\mathbf{Q}^{+-}] \end{pmatrix}\begin{pmatrix} \mathbf{E}^{+}(n) \\ \mathbf{E}^{-}(n+1) \end{pmatrix}$$
$$= \exp\left(i\mathbf{k}\times\mathbf{a}_3\right)\begin{pmatrix} \mathbf{E}^{+}(n) \\ \mathbf{E}^{-}(n+1) \end{pmatrix}$$

$$(12)$$

Here the matrices **Q** are the scattering matrices defined as $Q_{gg'}^{ss'} = M_{gg'}^{ss'} \exp\left[i\left(s\mathbf{K}_g^s \cdot \mathbf{d}_r + s'\mathbf{K}_{g'}^{s'} \cdot \mathbf{d}_l\right)\right]$ where s and s′ are + or − signs, g and g′ index the 2D reciprocal lattice vectors, $\mathbf{d}_r$ and $\mathbf{d}_l$ are right and left translation vectors, the matrix **M** is given in equation (11), and $\mathbf{a}_3$ is the primitive unit vector representing the periodicity in the 3rd dimension. It is noted that this last part is the standard transfer matrix formalism and can be used for non-spherical scatterers as well [45]. For given ω and $\mathbf{k}_{||}$ in the surface Brillouin zone, the matrix in equation (12) is fully specified and thus can be solved using the standard matrix inversion techniques. The plane wave expansion over the reciprocal lattice vectors of course will need to be truncated for numerical evaluations.

2.1.3 Effective medium theory

Now we explore the limiting cases where the multiple scattering theory presented above can either be simplified significantly or is inadequate. An obvious possibility of simplification is found when the interaction among the scatterers is weak. In this case, the multiple scattering effect will be small and may be ignored in the extreme case. A commonly employed approximation for such a case is the effective medium theory which attempts to obtain an average response of a non-uniform medium composed of multiple constituents. The most widely used effective medium theory is the Maxwell Garnett theory [46], which is derived from the Lorentz local field relation covered in many textbooks. Briefly, Lorentz considered an imaginary spherical cavity in a dielectric medium and stated that the local field is simply given by the sum of the dielectric response of the medium and the additional fields due to the surface charge on the spherical cavity and due to the atoms inside the cavity. The lattermost contribution cancels out to zero in a highly symmetric crystal structure. This leads to the famous expression,

$$\mathbf{E}_{local} = \mathbf{E} + \frac{4\pi\mathbf{P}}{3} \tag{13}$$

where **E** and **P** are the macroscopic field and polarization of the medium. Relating the local field to the induced atomic dipole moment, $\mathbf{p} = \alpha\mathbf{E}_{local}$, we arrive at the Clausius-Mossotti equation,

$$\frac{\varepsilon-1}{\varepsilon+2} = \frac{4\pi Na}{3} \tag{14}$$

where ε is the permittivity of the medium and N and α are atomic density and polarizability, respectively. Maxwell Garnett effective medium theory simply replaces the atomic polarizability in the Clausius-Mossotti equation with the polarizability of a spherical object. In the electrostatic limit, the polarizability of a sphere in vacuum has a simple form,

$$\alpha = \left(\frac{\varepsilon_s-1}{\varepsilon_s+2}\right)a^3 \tag{15}$$

where a is the radius of the spherical object and ε_s is the permittivity of the sphere. The Maxwell Garnett mixing rule is obtained by substituting equation (15) into (14),

$$\frac{\varepsilon-1}{\varepsilon+2} = f_s \cdot \frac{\varepsilon_s-1}{\varepsilon_s+2} \tag{16}$$

where f_s is the volume fraction of the sphere. For spheres embedded in a dielectric matrix with permittivity ε_m, we simply replace 1 and 2 in equation (16) with ε_m and $2\varepsilon_m$, respectively.

We now make a connection with the more rigorous multiple scattering theory presented earlier. In the Mie theory for a single spherical scatterer, the scattering coefficients a_n and b_n are generally expressed as infinite series of spherical Hankel functions. Using the power series expansions of the spherical Hankel functions, it can be shown that the leading terms of these coefficients are $a_1 \sim x^3$, $b_1 \sim x^5$, $a_2 \sim x^5$, $b_2 \sim x^7$, etc., where $x = 2\pi a/\lambda$. Therefore, for small spheres, we may retain only the leading term in a_1. Since the scattering and absorption cross sections are proportional to $|a_1|^2$ and $\mathbf{Im}(a_1)$ (imaginary part of a_1), respectively, the scattering and absorption efficiencies defined as the ratio of scattering and absorption cross sections to the physical cross section depend on x^4 and x, respectively, yielding the well-known Rayleigh scattering results. More specifically, the leading term of coefficient a_1 is

$$a_1 = -\frac{i2x^3}{3} \cdot \frac{\varepsilon_s-\varepsilon_m}{\varepsilon_s+2\varepsilon_m} \tag{17}$$

The relationship between the a_1 coefficient and the polarizability is apparent,

$$\alpha = \frac{3ia^3}{2x^3}a_1 \tag{18}$$

This relationship reveals one of the key approximations involved in the Maxwell Garnet effective medium theory: retaining only the leading term of the leading coefficient a_1 in the general solution of the Mie theory. This is essentially the electrostatic approximation in which the polarizability of small spheres is modeled by the static polarizability given in equation (15). A modest improvement on this approximation may be achieved by the extended Maxwell Garnett theory in which the full expansion of a_1 is used to calculate the polarizability [47]. The extended Maxwell Garnett theory has been used successfully for metamaterials [48,49]. However, if higher order terms in coefficient a_1 are to be included, it is logical to include b_1 and a_2

terms as well. These terms represent the contributions of the magnetic dipole and electric quadrupole terms, respectively. The inclusion of b_1 can be done straightforwardly by defining effective permeability in exactly the same way effective permittivity is calculated except that a_1 is replaced by b_1 to define magnetic polarizability. It has been shown that the optical properties of small particle composites may exhibit magnetic permeability even when the constituent materials are all non-magnetic [50]. Thus, the use of extended Maxwell Garnett theory is more appropriate when both effective permittivity and permeability are considered. It has also been attempted to improve the Maxwell Garnett theory using dressed polarizability to better account for the resonant effect [51]. In addition to neglecting higher multipole contributions to the light scattering and absorption, which is appropriate for small particles, the Maxwell Garnett effective medium theory also ignores multiple scattering among particles. This can be seen from the facts that the polarizability is defined by the single sphere Mie coefficient and that the effective permittivity is constructed based on the Lorentz local field concept. There are other issues related to the Maxwell Garnett effective medium theory such as the Lorentz catastrophe and non-symmetry and there exist other effective medium theories that improve on those shortcomings [52]. However, it can be said in general that the effective medium theory is appropriate for small particles with low volume fraction where both the higher order multipole contributions and inter-particle interaction by multiple scattering can be ignored.

2.1.4 Plasmon hybridization

We now us consider the opposite extreme where the particles are closely spaced and thus strongly interacting with one another. In this case, especially near plasmon resonances, strongly overlapping evanescent fields exist, leading to significant modification in the nature of the resonance. In principle, this near-field interaction can be described by the multiple scattering theory presented earlier. However, there is a practical difficulty in that it requires the inclusion of a large number partial waves and thus makes the numerical computation extremely challenging. Instead it is more profitable to look for new eigenmode solutions described by the collective modes delocalized over the entire structure. Prodan et al. proposed the plasmon hybridization model [13]. To be sure, the concept of plasmon hybridization itself is not new. A classic example is coupling of two surface plasmon modes in a metal thin film and the resultant formation of symmetric and anti-symmetric modes [53,54]. But Prodan's model is highly useful as it provides a complete set of eigenmode solutions in complex nanostructures. The plasmon hybridization model considers the electron gas as incompressible fluid subject to

Coulombic interaction. The plasmon resonance is then represented by self-sustained oscillations of the electron fluid which may be obtained from the Euler-Lagrange equation for the Lagrangian,

$$L = \frac{n_0 m}{2}\int \eta \nabla \eta dS - \frac{1}{2}\int \frac{\sigma(\mathbf{r})\sigma(\mathbf{r}')}{\mathbf{r} - \mathbf{r}'} dS dS' \qquad (19)$$

where n_0 and m are the electron density and mass, respectively, and σ is the surface charge density. This technique was shown to agree well with the full electrodynamic simulation results in the electrostatic limit where all of the involved length scales are small compared to the wavelength. It was successful in describing the plasmonic resonances in complex structures including nanoshell, nanoegg and nanorice [55]. The model has also been applied to multiparticle systems such as dimer, trimer, quadrumer, hexamer and heptamer [14,20,56]. A similar method has been proposed by Mayergoyz et al. who derived a boundary integral eigenvalue equation using the electrostatic approximation. In this approach, the surface plasmon resonance is described as an eigenstate of the homogeneous boundary integral equation [57],

$$\sigma(\mathbf{r}) = \frac{\gamma}{2\pi}\int \sigma(r')\frac{(\mathbf{r} - \mathbf{r}')}{|\mathbf{r} - \mathbf{r}'|^3}\cdot\hat{\mathbf{n}}dS \qquad (20)$$

For an arbitrary geometry, the boundary integral equation (20) can be solved numerically to obtain the eigenvalue γ and eigenfunction $\sigma(\mathbf{r})$. The eigenvalue γ is related to the permittivity $\varepsilon(\omega)$ of the metal as

$$\mathrm{Re}\varepsilon(\omega) = \varepsilon_b\left(\frac{1 + \gamma}{1 - \gamma}\right) \qquad (21)$$

where ε_b is the permittivity of the background material. It is thus possible to determine the resonance frequency from the permittivity of the metal. The eigenfunction $\sigma(\mathbf{r})$ describes the self-sustained surface charge distribution. This technique has been used to describe collective plasmon resonance supported by hexamers and heptamers made of gold nanoparticles and nanorods [17,21,22].

It should be noted that both of the two techniques described above employ electrostatic approximation and thus cannot describe the retardation effect. Their applicability is therefore limited to extremely small particles or low frequencies. Nevertheless, these methods proved highly useful in the exploration of coupled plasmon modes in complex nanostructures consisting of multiple nanoparticles. The main reason is the applicability of elegant group theoretical method in a fashion similar to the molecular orbital theory. Just as the molecular orbital can be constructed from the symmetry adapted linear combination of atomic orbitals, the hybridized plasmon modes can be constructed from the symmetry adapted linear combination of individual nanoparticle plasmon modes. This enables a

highly effective and systematic exploration of plasmon modes in a complex, strongly coupled nanostructure. Here we briefly describe this approach using the boundary integral method for a collection of nanoparticles. First, the plasmon modes of an isolated nanoparticle can be found from the eigenvalue equation given in (20). For the collection of N nanoparticles, the surface charge distribution can be expressed as a linear combination of the individual nanoparticle eigenmodes,

$$\sigma(\mathbf{r}) = \sum_{\alpha=1}^{N} \sum_{j} a_{\alpha}^{j} \sigma_{\alpha}^{j}(\mathbf{r}) \qquad (22)$$

Using equation (20), we may write

$$\sigma(\mathbf{r}) = \frac{\Lambda}{2\pi} \sum_{\beta,k} \int a_{\beta}^{k} \sigma_{\beta}^{k}(\mathbf{r}_{\beta}) \frac{(\mathbf{r}-\mathbf{r}_{\beta})}{|\mathbf{r}-\mathbf{r}_{\beta}|^{3}} \cdot \hat{\mathbf{n}} dS \qquad (23)$$

where σ_{β}^{k} represents the surface charge distribution of kth mode of βth nanoparticle. One can then use the bi-orthogonality between the surface charge distribution, $\sigma(\mathbf{r})$, and the surface dipole distribution, $\tau(\mathbf{r})$, to derive,

$$
\begin{aligned}
a_{n}^{m} &= \frac{\Lambda}{2\pi} \sum_{\beta,k} a_{\beta}^{k} \left\{ \int \tau_{\alpha}^{m}(\mathbf{r})\hat{\mathbf{n}} \cdot \int \sigma_{\beta}^{k}(\mathbf{r}_{\beta}) \frac{(\mathbf{r}-\mathbf{r}_{\beta})}{|\mathbf{r}-\mathbf{r}_{\beta}|^{3}} dS_{\beta} dS \right\} \\
&= \frac{\Lambda}{2\pi} \sum_{\beta,k} K_{\alpha\beta}^{mk} a_{\beta}^{k}
\end{aligned}
$$

$$(24)$$

The total surface charge distribution in equation (22) must satisfy the boundary integral eigenvalue equation in (20) where the integral is conducted over the surfaces of all nanoparticles. However, the problem now has been transformed to a matrix eigenvalue equation given in (24). Physically, the matrix $\mathbf{K}$ represents the interaction between the surface dipole density of the mth mode of α th particle and the charge distribution of the kth mode of βth particle. Now suppose the arrangement of the nanoparticles is symmetric and certain symmetry operations keep the nanoparticle cluster unchanged. This means the symmetry operators leave the interaction matrix $\mathbf{K}$ invariant. Then, the symmetry operators and matrix $\mathbf{K}$ commute and consequently they share the same eigenvectors. It is now possible to classify all eigenvectors of matrix $\mathbf{K}$ based on how they transform under various symmetry operations. In the language of group theory, the eigenvectors are classified by the irreducible representations of the symmetry group. These eigenvectors possess well-defined transformation characteristics under all symmetry operators that leave the structure invariant and form the symmetry-adapted basis set. The symmetry properties of the plasmon modes proved powerful in analyzing the interaction between various plasmon modes and also between light and plasmons.

For example, the incident light interacts with the surface plasmon mode via the induced dipole moment. For a given symmetry group, the dipole operator belongs to a certain irreducible representation. Thus, it naturally follows that only those surface plasmon modes belonging to the same irreducible representation as the dipole operator can interact with light. Other modes are the so-called dark modes that do not interact with incident light and thus cannot be detected by experiments. Furthermore, surface plasmon modes belonging to different irreducible representations do not mix together as their basis functions are mutually orthogonal. These properties provide powerful insights into how complex plasmon modes evolve and interact in complex nanostructures.

2.2 Weakly coupled plasmonic nanostructures

As discussed in the previous section, when the plasmonic nanostructures are only weakly coupled, they may be described well by the effective medium theory. There is a large body of literature on metamaterials which are composed of deep sub-wavelength scale structures and are generally described well by the effective medium theory. The initial development of metamaterials was driven largely by the negative index materials for which excellent reviews are available [58,59]. In this section, we focus on the latest development of plasmonic nanostructures in the weak coupling regime.
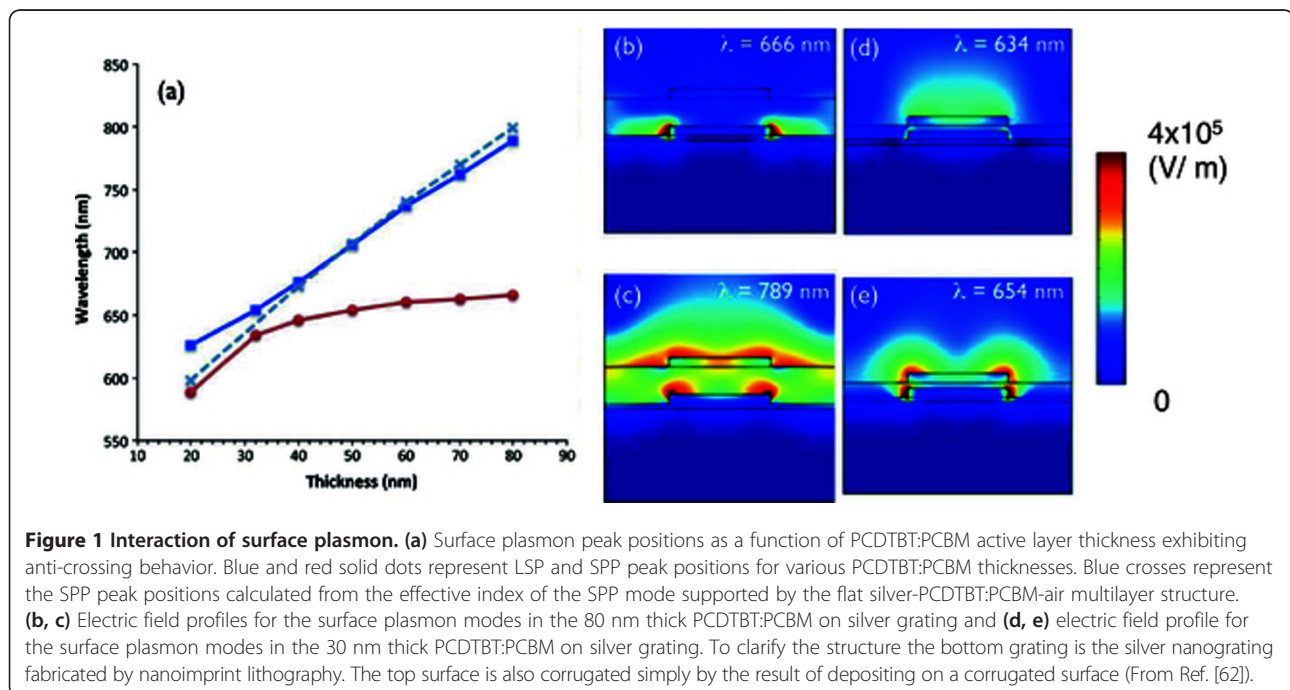
2.2.1 Perfect absorber

An interesting application of plasmonic nanostructures is the perfect absorber which absorbs all incident light with minimal reflection and transmission. Such a material would find a wide range of applications in, for example, coatings for optical instruments, sensors, and photo-thermal or photovoltaic energy conversion devices. An inspection of Fresnel's coefficients immediately reveals that perfect absorption is achieved when the real part of the refractive index is matched with the incident medium and the imaginary part is small. This condition would result in negligibly small reflection and, if the material is thick enough, vanishing transmission as well. This is, in fact, how perfectly absorbing metamaterial was obtained using aligned carbon nanotube arrays [60]. This example illustrates clearly that a perfect absorber does not have to involve a plasmonic nanostructure [60,61]. It is, however, of great technological importance to achieve perfect absorption in thin films and plasmonic nanostructures are ideally suited for that purpose.

One of the simplest examples is a line grating. It is well known that a line grating on a metal surface can couple the free space light into surface plasmons. An ideal grating presents infinitesimal modulation of surface so that the plasmon modes of the original flat surface are well preserved and the grating only provides the

extra momentum for coupling. However, it was found that, even in a grating as shallow as 20 nm, additional surface plasmon modes strongly localized at the grating lines exist and interact with the surface plasmon-polariton modes. Lu et al. investigated silver nanograting structures fabricated on the back-electrode of a PCDTBT:PCBM organic photovoltaic device [62]. The system supports two surface plasmon modes when excited by transverse-magnetic (TM, electric field perpendicular to the grating lines) polarized incident light. One is the localized surface plasmon (LSP) mode whose field profile is strongly localized at the grating lines and wavelength insensitive to the incident angle and active layer thickness. The other is the surface plasmon-polariton (SPP) mode strongly interacting with the grating period and thus highly sensitive to incident angle and active layer thickness. Figure 1(a) shows the wavelength of surface plasmon induced absorption peaks as a function of active layer thickness, revealing two branches with distinct dependence on active layer thickness. In general, as the active layer thickness is increased, the refractive index of the dielectric side of the surface is increased, resulting in a red shift in surface plasmon wavelength. The surface plasmon dispersion relation for a dielectric loaded metal surface can be calculated numerically [34]. As shown by the light blue crosses in Figure 1(a), the surface plasmon wavelength exhibits a red shift with increasing active layer thickness and this line coincides well with the SPP branch of the silver nanograting overcoated with PCDTBT:PCBM active layer. This indicates that the 20 nm tall silver nanograting acts as an ideal grating for the SPP modes which retain the characteristics of those in the flat dielectric loaded metal surface. The other branch representing LSP modes is unique to the grating structure and not observed in flat interfaces. Due to the strongly localized nature, it is insensitive to the thickness of the dielectric layer. For thicknesses near 30 nm, the two branches exhibit anti-crossing, indicative of strong mixing between the LSP and SPP modes. The field profiles in Figure 1(b) and (c) show the two contrasting patterns for LSP and SPP modes while those in Figure 1(d) and (e) reveal considerable mixing. Since these modes strongly affect the absorption spectra, the knowledge of the existence of two different modes and their interaction is essential to designing light trapping plasmonic grating structures for photovoltaic devices.

When the grating height is increased, the surface plasmons lose their original characteristics of flat interfaces and the LSP modes become the dominant features. Kravets et al. studied a gold grating with 130 nm height fabricated by depositing gold on a 130 nm thick poly(methyl methacrylate) (PMMA) grating [63]. As shown in Figure 2, this structure exhibited extremely low reflectance and transmittance for TM polarized light, achieving blackbody-like absorption in the visible spectrum with a thickness much smaller than the wavelengths. A theoretical analysis is needed to understand this remarkable behavior. A rigorous theoretical treatment would require full consideration of two sets of gold gratings, one formed in between the PMMA lines and another formed on top of PMMA lines.
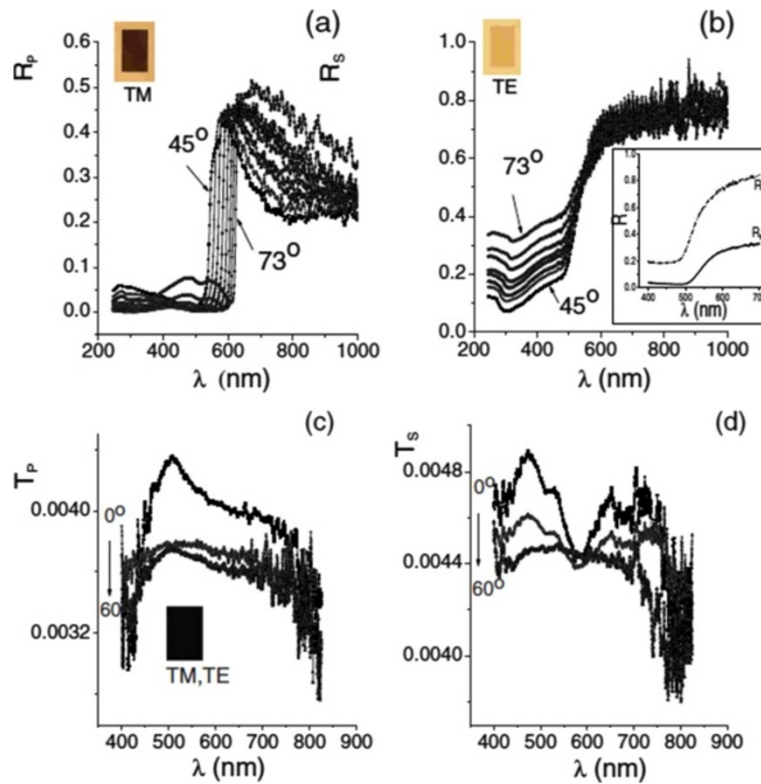

Figure 1 Interaction of surface plasmon. **(a)** Surface plasmon peak positions as a function of PCDTBT:PCBM active layer thickness exhibiting anti-crossing behavior. Blue and red solid dots represent LSP and SPP peak positions for various PCDTBT:PCBM thicknesses. Blue crosses represent the SPP peak positions calculated from the effective index of the SPP mode supported by the flat silver-PCDTBT:PCBM-air multilayer structure. **(b, c)** Electric field profiles for the surface plasmon modes in the 80 nm thick PCDTBT:PCBM on silver grating and **(d, e)** electric field profile for the surface plasmon modes in the 30 nm thick PCDTBT:PCBM on silver grating. To clarify the structure the bottom grating is the silver nanograting fabricated by nanoimprint lithography. The top surface is also corrugated simply by the result of depositing on a corrugated surface (From Ref. [62]).

Figure 2 Reflectance and transmittance spectra of the gold nanostripe array with period = 320 nm and linewidth = 150 nm. Insets show the polarization-contrast optical microscopy images. The inset in **(b)** shows reflectance spectra for s- and p-polarizations at normal incidence (From Ref. [63]).

However, since the grating lines are well separated (by more than 100 nm), near-field coupling between adjacent grating lines should be small and therefore it should be possible to use a much simpler effective medium theory. To generalize the Maxwell Garnett results for spherical particles given in equations (14) ~ (16) to non-spherical shapes, we introduce depolarization factor, L. For a general ellipsoidal shape, L is defined as [64]

$$L_i = \frac{a_x a_y a_z}{2} \int_0^\infty \frac{dS}{(s+a_i^2)\sqrt{(s+a_x^2)(s+a_y^2)(s+a_z^2)}} \quad \text{where}$$
$$i = x, y, z \tag{25}$$

where a_i is the semi-axis along the i-direction. For a sphere, $L_x = L_y = L_z = 1/3$. For a cylinder oriented along the x-direction, $L_x = 0$, $L_y = L_z = 1/2$. For a thin film in the yz plane, $L_x = 1$, $L_y = L_z = 0$. We can now write a generalized Maxwell Garnett effective permittivity as follows [65].

$$\varepsilon_{eff}^i = 1 + \frac{f\alpha_i}{1 - fL_i\alpha_i} \quad \text{where} \quad i = x, y, z \tag{26}$$

where f is the volume fraction as before. Furthermore, the volume-normalized polarizability can be written in terms of the depolarization factor as,

$$\alpha_i = \frac{\varepsilon_s/\varepsilon_m - 1}{1 + L_i(\varepsilon_s/\varepsilon_m - 1)} \quad \text{where} \quad i = x, y, z \tag{27}$$

where ε_s and ε_m are the permittivity of the ellipsoid and medium, respectively. Combining the two equations above yields

$$\alpha_z = \varepsilon_s/\varepsilon_m - 1 \quad and \quad \alpha_y = \alpha_z \frac{2(\varepsilon_s/\varepsilon_m - 1)}{\varepsilon_s/\varepsilon_m - 1} \tag{28}$$

$$\varepsilon_{eff}^x = 1 + f(\varepsilon_s/\varepsilon_m - 1) \quad and$$
$$\varepsilon_{eff}^y = \varepsilon_{eff}^z \frac{\varepsilon_s/\varepsilon_m - 1 + f(\varepsilon_s/\varepsilon_m - 1)}{\varepsilon_s/\varepsilon_m + 1 - f(\varepsilon_s/\varepsilon_m - 1)} \tag{29}$$

for a cylinder oriented along the x-axis. Equation (29) yields the real and imaginary parts of the effective refractive index of the gold grating to be roughly 1.5 and 0.3, respectively, over a broad wavelength range up to 500 nm for TM polarization. These values are close to the optimal complex refractive index value for near-perfect absorption in a thin film. For example, a film with 130 nm thickness on a glass substrate would exhibit

90% absorption at $\lambda = 400$ nm if the refractive index is $1.3 + 0.5i$. A similar approach can be made with nanoparticles instead of nanograting [66]. In this case, the polarizability of a sphere given in equation (15) in Section 2.3 can be used in the Maxwell Garnett effective medium theory. The major difference in the nanoparticle composite medium and the nanograting is the polarization dependence. The inherent isotropy of spherical geometry naturally leads to isotropic, polarization-independent medium in contrast to the strong polarization sensitivity in nanogratings.

A question of both scientific and technological interest is how much absorption is possible in ultrathin films. A simple solution may be found by using total internal reflection. Using the Kretschmann geometry, an ultrathin film absorber can be excited at glancing angle, effectively extending the optical path to infinity and consequently achieving near-perfect absorption. Using this method, 94% absorption in a 4.5 nm thick NbN nanowire array has been demonstrated [67]. It should be noted that this method does not require surface plasmon or any other types of surface resonances, although they could certainly help. While this approach clearly offers a quick solution to achieve perfect absorption, it is not always possible or feasible to use total internal reflection geometry and it would be much more desirable to achieve high absorption at normal incidence or over a broad range of incident angles. To tackle this problem, let us consider a thin film with thickness d and refractive index $m = n + i\kappa$ on a semi-infinite substrate with refractive index n_s and incident medium with refractive index n_i (Figure 3a). The reflection

and transmission coefficients for normal incidence can then be written in a general form as follows.

$$r = \frac{r_i - r_s\gamma^2}{1 - r_i r_s \gamma^2} \quad and \quad t = \frac{(1+r_i)(1+r_s)\gamma}{1 - r_i r_s \gamma^2} \exp(-in_s\delta)$$
$$where \quad r_{i,s} = \frac{n_{i,s} - m}{n_{i,s} + m} \quad and \quad \gamma = \exp(im\delta)$$

$$(30)$$

Also, $\delta = q_0 d$ and q_0 is the vacuum wave number. Generalization to non-normal incidence is straightforwardly done by replacing q_0 with the normal component of incident wave vector. The absorptance is given by where $C = n_s/n_i$ for transverse-electric (TE) incident field and for TM. One can now survey the possible values of m to find the maximum absorption. Figure 3(b ~ e) shows the absorptance at $\lambda_0 = 900$ nm for various film thicknesses of 2, 10, 50 and 150 nm. All cases show a maximum absorptance of approximately 50% along the line $n = \kappa$. Thick films show additional maxima along the horizontal axis due to the Fabry-Perot resonances. In ultrathin films, only those maxima occurring along $n = \kappa$ line are achievable. Normally, for a fixed value of m, the absorption vanishes with vanishing thickness as $A = O(\delta)$. To go beyond this limit, Hägglund et al. sought a refractive index value with dependence where $-1 < \nu < 0$ so that m is large enough to produce substantial absorption while remains small [68]. The optimum value of m_{max} resulting maximum absorption was given as,
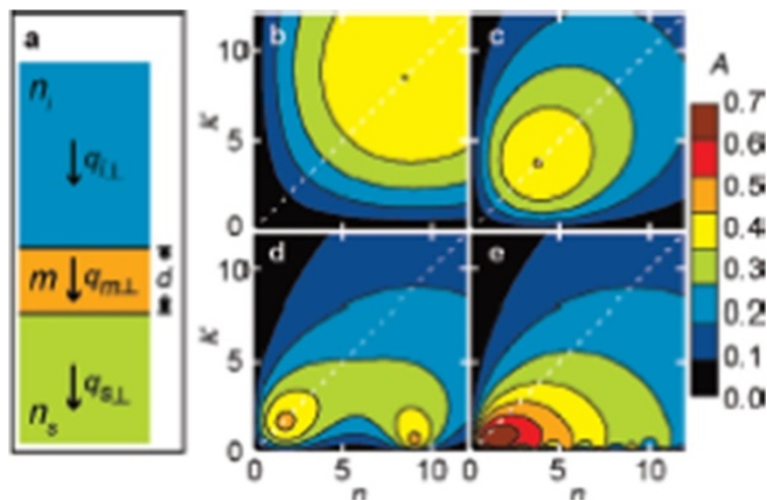

Figure 3 Absorptance of thin film with complex refractive index. (a) Thin homogeneous film with complex refractive index m = n + iκ and thickness d is embedded between two semi-infinite dielectrics of refractive indices n_i and n_s, respectively. In **(b-e)**, absorptance in the film is shown as a function of its optical constants for normal incident light. The wavelength is 900 nm, and the dielectric environment has $n_i = n_s = 1$. The film thicknesses d are 2, 10, 50, and 250 nm in panels **b**, **c**, **d**, and **e**, respectively. The dotted lines mark n = κ about which the shown absorption is nearly symmetric for the two thinnest films **(b, c)**. In these cases, the absorptance reaches a peak value of close to 50% on the symmetry line. For the two thicker films **(d, e)**, the peak height increases and additional maxima appear along the n-axis due to Fabry-Perot modes (From Ref. [68]).

$$m_{max} = \frac{1+i}{\sqrt{2}} \left(\frac{n_i + n_s}{\delta}\right)^{1/2}$$
$$+ \frac{1+i}{6\sqrt{2}} \frac{(n_i^3 + n_s^3)}{(n_i + n_s)^{3/2}} \delta^{1/2} + O(\delta^{3/2}) \qquad (31)$$

The maximum absorptance is given as

$$A_{max} = \frac{n_i}{n_i + n_s} \left[1 + \frac{n_s}{6}(3n_s - n_i)\delta^2\right] + O(\delta^4) \qquad (32)$$

Equations (31) and (32) show that the maximum absorption occurs at $n = \kappa$ and the maximum absorptance is close to 50%, both of which are shown in Figure 3.

It is obvious that no natural materials would exhibit the optimum refractive index given in equation (31). It is therefore necessary to create a composite medium whose effective refractive index is close to the optimum. It was shown that 50% absorptance could be realized over a broad range of wavelengths using an array of ellipsoidal silver shells with various geometry [68]. This scheme can be extended to a thin film with a back reflector. The reflector automatically eliminates transmission and the problem is reduced to minimizing reflectance. A general system to consider is an ultrathin film with a complex refractive index m and thickness d, separated from a perfect reflector by a spacer layer with refractive index n_s and thickness h. The incident medium index is n_i. The reflection coefficient is then given as

$$r = \frac{r_i - r_d\gamma^2}{1 - r_i r_d \gamma^2} \qquad (33)$$

where $\quad r = \frac{n_{i,d} - m}{n_{i,d} + m}, \quad \gamma = \exp(im\delta)$ and

$$n_s = in_s \ \cot(\pi\lambda_c/2\lambda)$$

The critical wavelength λ_c is defined as the wavelength satisfying the quarter wavelength condition, $\lambda_c = 4n_s h$ Equation (33) has the same form as equation (30) and thus $\tilde{n}_s$ may be treated as the effective index of the spacer-reflector system. The maximum absorption condition is then found by requiring $r_i = r_d\gamma^2$ in equation (33). Retaining only the leading term the optimum refractive index is given as [69],

$$m^2 \quad = \frac{i(n_i - .n_s)}{\delta} \quad = \frac{\lambda}{2\pi d}\left[in_i + n_s \cot\left(\frac{\pi\lambda_c}{2\lambda}\right)\right] \qquad (34)$$

When $\lambda = \lambda_c$, $\tilde{n}_s = 0$ and the optimum refractive index is given as $m = (1+i)\sqrt{n_i/2\delta}$. This represents the critical coupling condition where the required refractive index m is minimum. On the other hand, when the spacer layer thickness tends to zero, n_N diverges and the optimum refractive index cannot be satisfied. Again, the implementation of this concept requires an artificial composite medium made of plasmonic nanostructures. Recently, strong absorption has

been experimentally observed using a gold nanoparticle array fabricated by block copolymer lithography and overcoated with a dielectric layer by atomic layer deposition [70]. As shown in Figure 4, the ultrathin composite film with a thickness of ~25 nm exhibited near-perfect absorption at around 600 nm. Vast majority of absorption occurs in the gold nanoparticles, which is not desirable for photovoltaic applications where the absorption must take place in the semiconducting material for current extraction. It is nevertheless noteworthy that the effective absorption coefficient of the gold nanoparticles in this structure was an order of magnitude greater than solid metal. A similar critical coupling leading to perfect absorption has been reported on a gold nanodisk array deposited on a glass substrate [71]. In this case, the critical coupling condition was achieved by tuning the nanodisk density and incident angle of incoming light. When the critical coupling condition is satisfied, reflected light is annihilated by the destructive interference between the light reflected from the substrate and the gold nanodisk array layer.

2.2.2 Invisibility

In addition to enhancing absorption, controlling or suppressing light scattering is also of great interest for many applications. It has been shown that the dominant dipolar contribution to the scattering from a spherical or cylindrical dielectric object could be greatly reduced when coated by a layer of material with negative or very low values of the real part of permittivity [72]. This technique is inherently non-resonant and thus the bandwidth of the scattering cancellation can be quite broad and limited only by the material dispersion of the coating. It was shown that the operational bandwidth could be further extended by use of multiple layers of coatings [73]. Potential applications of this type of cloaking include cloaked sensors [74], cloaked near-field probes [75,76] and reduction of optical forces [77]. For implementation, a natural choice for the coating material is a metal, which exhibits negative permittivity values at frequencies below its plasma frequency. However, in the optical frequency region, most metals tend to exhibit large negative permittivity values. Consequently, an unrealistically thin layer is required to cancel the dipole moment of a dielectric object whose permittivity is typically a small positive number. To circumvent this issue, an effective medium formed by plasmonic nanostructure is needed. Recently, Tamma et al. reported scattering cancellation by a gold nanograting fabricated on the sidewall of a silicon nanorod [78]. As shown in Figure 5(a), the cloaked object was a silicon nanorod fabricated by electron-beam lithography. The gold nanograting was then fabricated on the sidewall by a combination of gold evaporation, focused ion beam milling and silica protective coating deposition by sputtering. The final structure was coated with SU-8 to form a
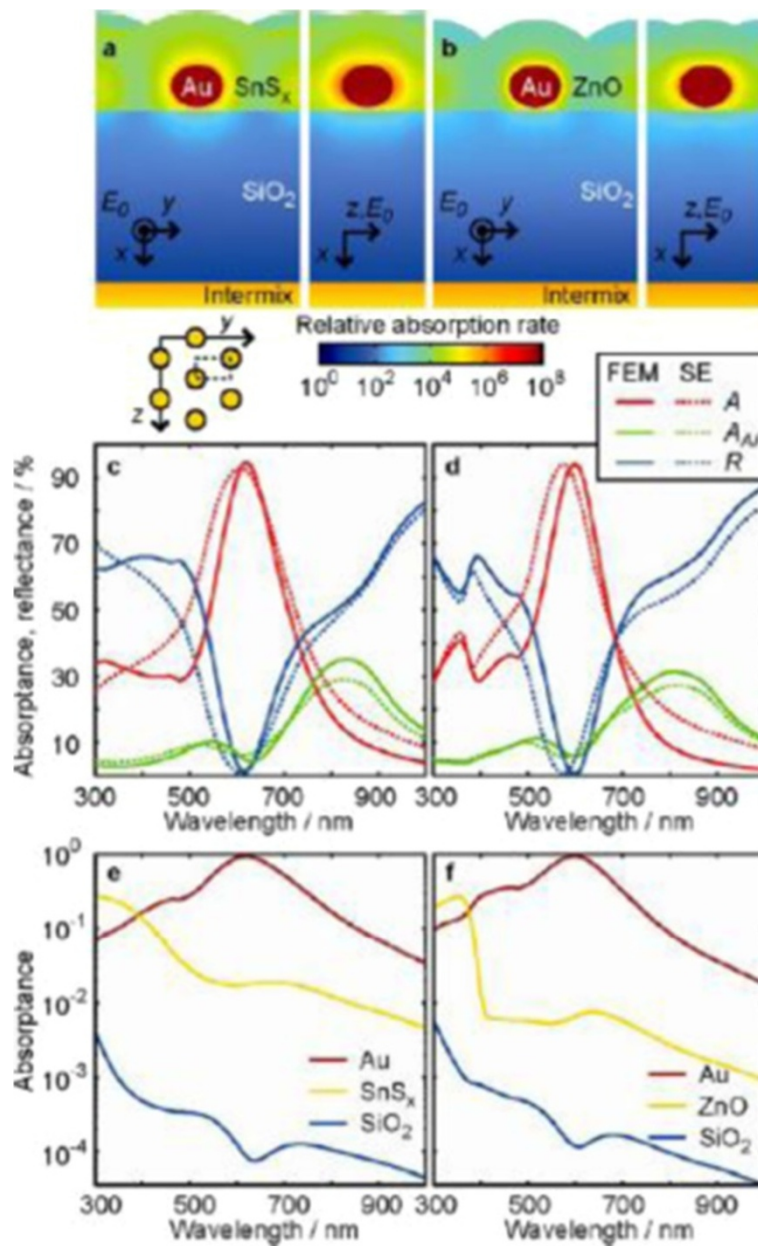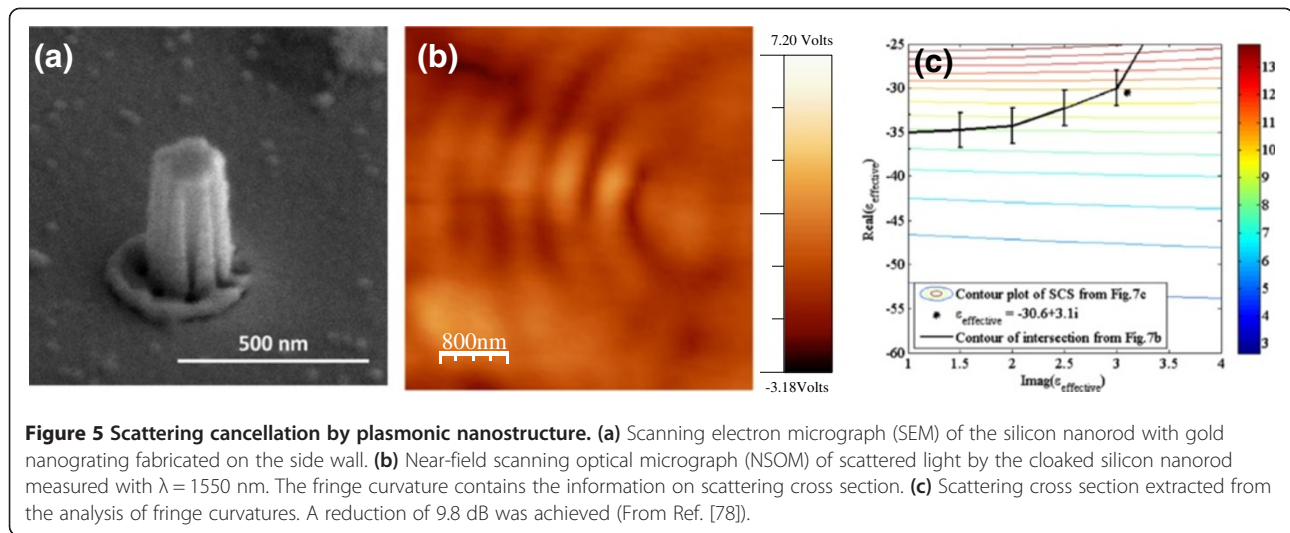
Figure 4 Absorptance of gold nanoparticle embedded thin films. (a) Finite element method (FEM) calculated absorption rates, determined for the sample with the highest absorbing SnS_x coated Au array at its peak wavelength. A plane wave with incident electric field strength E_0 propagates along the normal (x-) direction, with its electric field vector along z. The rectangular unit cell used for the hexagonal lattice is shown below the plot (dashed lines). **(b)** Analogous for ZnO coated sample. **(c, d)** Sample reflectance (R), array absorptance (A), and absorptance in the Al reflector (AAl, including intermix layer), as calculated by FEM and obtained from the spectroscopic ellipsometry (SE) model. **(e)** FEM calculated absorptance in the Au dots of the SnS_x coated sample, in the SnS_x coating, and in the SiO_2 spacer, respectively. **(f)** Analogous for the ZnO coated sample (From Ref. [70]).

waveguide layer and the structure was excited by 1550 nm light coupled into the SU-8 guiding layer. The scattering properties were then investigated by near-field scanning optical microscopy (NSOM). The waveguide geometry used in this study makes it impossible to directly measure the scattered light intensity. Instead, NSOM was used to map the interference fringes produced by the incident light and back-scattered light (Figure 5b). It was clear that the cloaked silicon nanorod scattered much less because the interference fringes were weak and required a long integration time and high gain to obtain reliable data whereas the reference nanorod showed a strong interference pattern. Tamma et al. then used the effective medium theory to relate the effective index of the coating with the

Figure 5 Scattering cancellation by plasmonic nanostructure. (a) Scanning electron micrograph (SEM) of the silicon nanorod with gold nanograting fabricated on the side wall. **(b)** Near-field scanning optical micrograph (NSOM) of scattered light by the cloaked silicon nanorod measured with λ = 1550 nm. The fringe curvature contains the information on scattering cross section. **(c)** Scattering cross section extracted from the analysis of fringe curvatures. A reduction of 9.8 dB was achieved (From Ref. [78]).

fringe curvature. Here the gold nanograting coating was described as a multilayer structure for which the effective medium theory simple yields [79]

$$\varepsilon_{\parallel} = f_a \varepsilon_a + f_b \varepsilon_b \quad and \quad \varepsilon_{\perp} = (f_a/\varepsilon_a + f_b/\varepsilon_b)^{-1}$$

(35)

where the subscripts || and ⊥ indicates polarization parallel and perpendicular to the interface, respectively. The result of the complete analysis shown in Figure 5(c) indicates that a 9.8 dB reduction in scattering cross section has been achieved. The same approach has been implemented with silver nanoparticles attached on silica spheres [80]. The scattering reduction was however small, ~20%, and the system also exhibited strong absorption.

In concluding the discussion on weakly coupled system that can be described well by the effective medium theory, it is worth noting the robustness of effective medium theory. As discussed in the previous section, the effective medium theory is valid only when the feature size is small compared to the wavelength and the interaction among the nanostructures is weak. When these two conditions are met, the optical properties of the composite structure are determined by the dipole moment of the individual nanostructure without having to include higher order resonances and any higher order interaction. These conditions certainly sound very restrictive but in reality the effective medium theory has been successfully applied to a wide variety of systems which at first glace do not seem to satisfy the conditions for validity. An excellent example is the silicon nanorod cloaked by an array of gold nanowires described above. The individual gold nanowire was 13 nm thick and 20 nm wide and the spacing between two adjacent gold nanowires was 63 nm. This system was modeled as a multilayer composed of 20 nm thick gold and 43 nm thick silica films. Despite this seemingly gross simplification, the effective medium theory provided a remarkably accurate result in good agreement with experiments. It can be argued that the effective medium theory, although oversimplified, has captured the essential part of the light-matter interaction, which in this case concerns the induced surface charge and resultant screening effect. The effective medium theory for multilayers resulting in effective permittivity given in equation [35] considers the induced polarization in each layer. When the incident electric field is perpendicular to the multilayer interfaces, it produces a net interface charge due to the discontinuity in permittivity at the interface. These interface charges then produce a polarization field that counteracts the incident electric field, resulting in a permittivity given as $\varepsilon_{\perp}$ in equation [35]. On the other hand, when the incident electric field is parallel to the interface, no interface charge is formed and thus the effective permittivity is simple given as an arithmetic mean of the constituent permittivities, as given for $\varepsilon_{\parallel}$ in equation [35]. The experiments in the cloaked silicon nanorod were done for TM waveguide mode which has electric field parallel to the gold nanowires. This corresponds to the no interface charge case and the multilayer effective medium theory for no screening case is applicable. If the experiments were done for perpendicular polarization, it would have been important to accurately account for the interface charge density and thus the multilayer effective medium theory could have been inaccurate.

Another case worth mentioning is the nanoparticle array. It is well established that small nanoparticles have dominantly dipole character with negligible contributions by the high order components. Thus, as long as the nanoparticles are separated well enough, effective medium theory should work well. But defining a precise validity limit is difficult because unlike the perturbation theory the effective medium theory does not allow quantitative estimation of errors. For

plasmonic nanoparticles, the literature suggests volume fraction of 10 ~ 20% would be the upper limit where the effective medium theory begins to break down [49,81]. In a study of collective magnetic resonance supported by a cluster of plasmonic nanoparticles, Tamma et al. presented a comparison between the rigorous multiple scattering theory and the extended Maxwell Garnett effective medium theory [49]. Figure 6 shows the dispersion curves and effective permittivity for silver nanoparticle arrays with silver volume fractions of 0.1, 0.3 and 0.5. As shown, even at a very high volume fraction of 0.5, the effective medium theory agrees reasonably well with the rigorous multiple scattering theory. The discrepancy is found near the band edge in all cases where the discrepancy remains small for f = 0.1 and becomes significant for higher volume fractions. This discrepancy observed near the band edge captures the nature of approximation in the effective medium theory. Unlike the effective medium theory, the multiple scattering formalism requires the complete knowledge of the nanoparticle positions in the array. For the calculations in Figure 6, the nanoparticles were assumed to be in the face-centered cubic (fcc) structure and the light propagation along the (111) direction was calculated. If the calculations were made for other crystallographic directions, the resulting dispersion curves would be different and the differences would be most pronounced near the band edge where the Bragg resonance condition is met. By construction, the effective medium theory does not require the knowledge of nanoparticle arrangement. This implies the effective medium theory would represent an averaged response of all different crystallographic orientations. It is therefore not surprising to see the major difference between multiple scattering theory and effective medium theory near the band edge. This however does not necessarily represent the deficiency of effective medium theory because most nanocomposite structures do not have a definite crystal structure. A few exceptions are DNA-driven self-assembly of plasmonic nanoparticles that lead to single crystalline fcc and body-centered cubic structures [82,83]. But even in those cases, the achievable structures remain small and multiple crystallographic orientations may be in play. Therefore, although it is advisable to compare with rigorous multiple scattering or other methods whenever possible, the effective medium theory remains highly useful in an extremely wide range of plasmonic nanostructures.

2.3 Strongly coupled plasmonic nanostructures
2.3.1 Dimers
Strongly coupled plasmonic nanostructures have been studied extensively during the past decade. For example, the hot spot leading to enhanced Raman scattering is generally attributed to the coupling between two adjacent silver nanoparticles producing strong local field in the gap between the two nanoparticles [84]. A similar
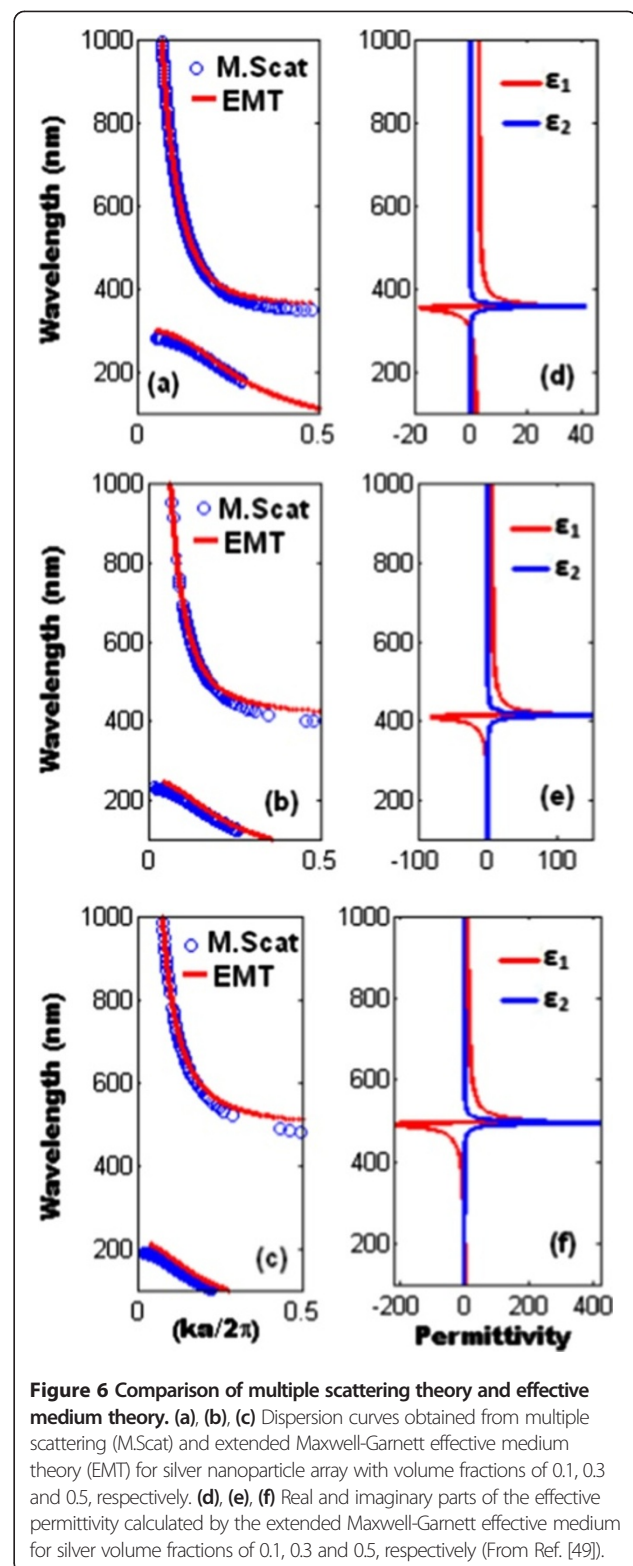

Figure 6 Comparison of multiple scattering theory and effective medium theory. (a), **(b)**, **(c)** Dispersion curves obtained from multiple scattering (M.Scat) and extended Maxwell-Garnett effective medium theory (EMT) for silver nanoparticle array with volume fractions of 0.1, 0.3 and 0.5, respectively. **(d)**, **(e)**, **(f)** Real and imaginary parts of the effective permittivity calculated by the extended Maxwell-Garnett effective medium for silver volume fractions of 0.1, 0.3 and 0.5, respectively (From Ref. [49]).

phenomenon has been observed in a coupled-dipole nano-antenna composed of two nanorods aligned end-to-end and separated by a small gap [85]. Also, early experimental studies on the simple model system of two closely spaced

metal nanoparticles, a system often dubbed as dimer, showed the plasmon resonance exhibits red shift with decreasing gap between the nanoparticles [86-89]. Both the formation of hot spots and the red shift with decreasing gap size are due to the hybridization of individual nanoparticle plasmons. When the gap between the nanoparticles is small enough to allow significant overlap of the plasmon modes of the individual nanoparticles, the strong near-field interaction consequently leads to hybridization of the individual single particle plasmon modes to form a new set of coupled modes delocalized over the entire structure. In a dimer, the single particle plasmon modes couple with each other to form symmetric and anti-symmetric combinations. This is the standard coupled oscillator problem with numerous analogous examples in physics [90]. In the plasmonic dimer, the oscillating entity is the free electron charge in the metal. When the charge density in the two particles oscillates in phase along the axis of the dimer, we have a symmetric mode with strong electric field in the gap. When the two oscillations are 180° out of phase, we have an anti-symmetric mode whose electric field profile has a null in the gap. In molecular analogy, the symmetric mode corresponds to the bonding orbital whereas the anti-symmetric mode is the anti-bonding orbital. Also, the symmetric mode has a lower energy and the anti-symmetric mode has a higher energy, just as the bonding orbital has a lower energy and the anti-bonding orbital has a higher energy. As illustrated in Figure 7 for a nanorod dimer, this hybridization model offers a good explanation for both the hot spot formation and the red shift in plasmon resonance wavelength.

The hybridized plasmon modes in a dimer can be monitored by directly solving Maxwell's equations numerically using techniques such as finite-difference time-domain (FDTD) [91] or finite-element method (FEM) [92]. Nevertheless, it is always profitable to seek for a theoretical model that could provide deeper insights on the physics governing the hybridization. Also, it is worth mentioning the inability of most brute force numerical simulations to excite anti-symmetric modes. This deficiency stems from the typical simulation geometry in which the nanostructure under investigation is excited by incident light. The simulation then calculates the resultant absorption or scattering which reveals the characteristics of the hybridized plasmon modes. This unfortunately works well only for the symmetric mode, which typically possesses a large dipole moment and thus interacts strongly with light. The anti-symmetric mode, however, represents a state in which the induced dipole moments in the individual nanoparticles align anti-parallel and thus only produce a small net dipole moment. This mode therefore does not interact with light and remain invisible in most experiments and simulations. For this reason, the symmetric mode is often referred to as the bright mode and the anti-symmetric mode as the dark mode. The
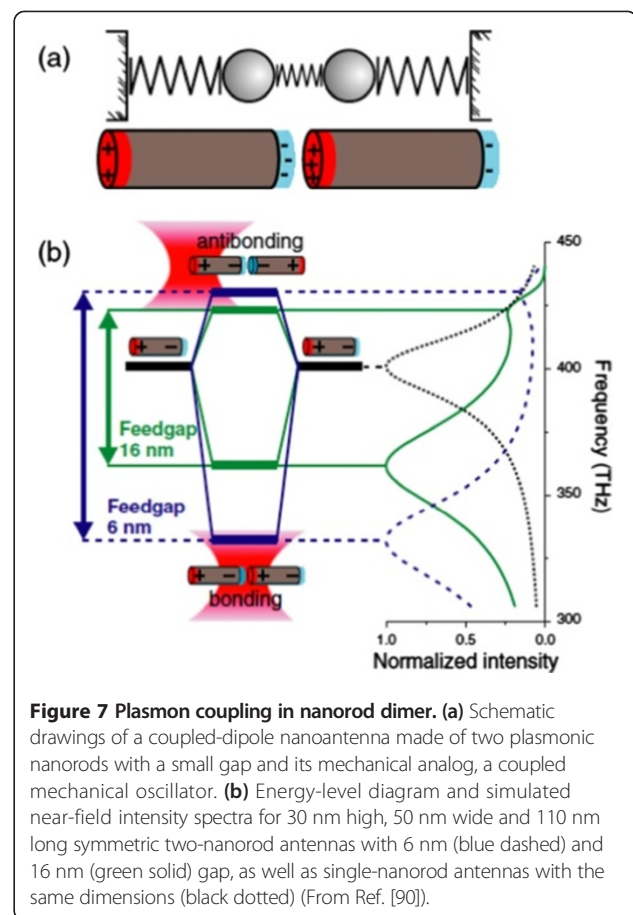

Figure 7 Plasmon coupling in nanorod dimer. (a) Schematic drawings of a coupled-dipole nanoantenna made of two plasmonic nanorods with a small gap and its mechanical analog, a coupled mechanical oscillator. (b) Energy-level diagram and simulated near-field intensity spectra for 30 nm high, 50 nm wide and 110 nm long symmetric two-nanorod antennas with 6 nm (blue dashed) and 16 nm (green solid) gap, as well as single-nanorod antennas with the same dimensions (black dotted) (From Ref. [90]).

anti-symmetric mode is nonetheless important as, for example, it can interact with the bright mode to produce Fano resonance as described later. It is therefore useful to have a theoretical model that can describe both the symmetric and anti-symmetric modes equally well. The simplest model employs the electrostatic approximation where the retardation effects are neglected. In this formalism, the polarizability, α, of individual nanoparticles is given by equations (15) and (27) for spheres and ellipsoids, respectively. The induced dipole moment in each particle is then given as $\mu = \alpha E$. In a dimer, the field, E, contains both the applied field and the field produced by the neighboring particle. Since an individual nanoparticle is treated as a point dipole, we can write

$$\mathbf{E}_1 = \mathbf{E}_{inc} + g \cdot \frac{\mu_2}{\varepsilon_m d^3} \quad \text{and} \quad \mathbf{E}_2 = \mathbf{E}_{inc} + g \cdot \frac{\mu_1}{\varepsilon_m d^3} \qquad (36)$$

Here the subscripts 1 and 2 index the two particles in the dimer, ε_m is the permittivity of the background medium and g is the geometry dependent parameter given as $g = 2$ for end-to-end coupling and $g = -1$ for side-to-side coupling [93,94]. The coupled equation

in [36] can be solved to find the polarizability of the bonding mode,

$$\langle \alpha \rangle = \frac{1}{2} \cdot \frac{\alpha_1 \left(1 + g\alpha_2/d^3 \right) + \alpha_2 \left(1 + g\alpha_1/d^3 \right)}{1 - g^2 \alpha_1 \alpha_2/d^6} \qquad (37)$$

The plasmon resonance condition is found by the maximum polarizability and, if the two particles are identical, is given as,

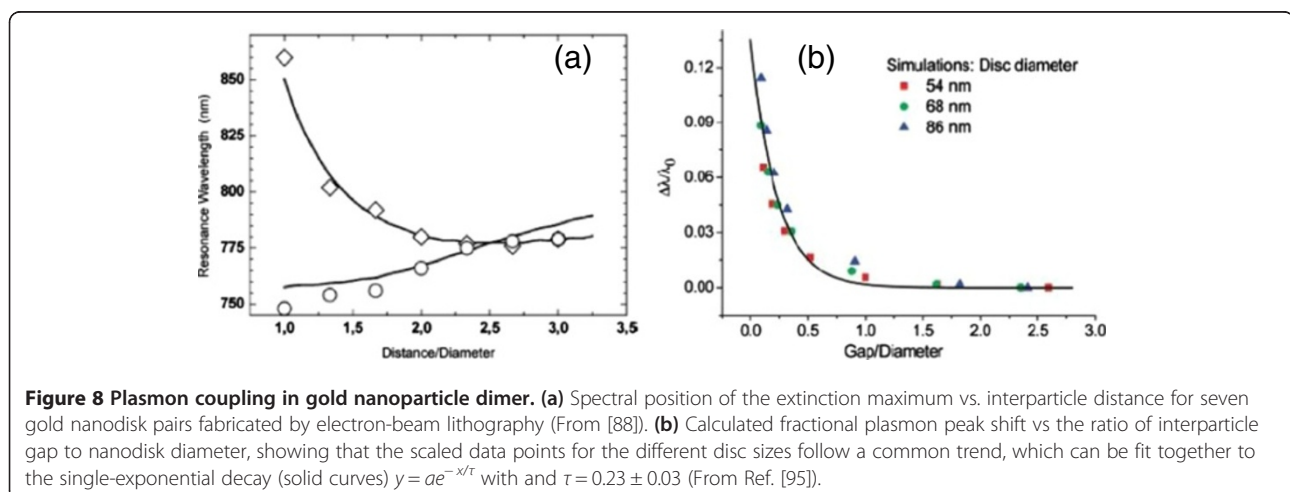$$\alpha = \frac{d^3}{g} \qquad (38)$$

Using the polarizability given in equation (27), we find

$$\frac{\varepsilon_s}{\varepsilon_s} = \frac{1 + d^3(1 - L_i)/g}{1 + d^3/g} \qquad (39)$$

Since the permittivity of gold has almost linear dependence on wavelength in the visible region, equation (39) specifies the dependence of the surface plasmon wavelength of a gold dimer on the center-to-center spacing. This simple model correctly predicts the red shift of the symmetric mode for end-to-end aligned dipole pair and the blue shift for side-to-side aligned dipole pair. The opposite behavior originates from the opposite sign of g in equations (37) ~ (39). In plasmonic dimer made of two identical particles, the end-to-end dipole alignment corresponds to the excitation of dimer with incident polarization along the dimer axis while the side-to-side coupling case corresponds to incident polarization perpendicular to the dimer axis. The opposite peak shifts in the two cases have been experimentally observed in the extinction spectra of gold nanodisk pairs fabricated by electron-beam lithography (Figure 8a) [88]. Furthermore, Jain et al. reported the fractional plasmon peak shift, $\Delta\lambda/\lambda_o$, exhibits a universal scaling against the normalized gap width defined as gap/diameter, irrespective of the

detailed geometrical parameters, as shown in Figure 8(b) [95]. This universal scaling was also found for dimers of non-circular shapes and nanoshells and also in trimers [96,97]. The origin of the universal scaling behavior may be found in equation (39), which predicts that the fractional peak shift would behave as $(d/D)^{-3}$ or $[(s + D)/D]^{-3}$ where $s = d - D$ is the gap width between the particles and D is the diameter. When the gap width becomes extremely small, the simple dipole-dipole interaction model breaks down and one must take into account the higher order multipole terms, leading to an exponential dependence observed in Figure 8. This omission of multipole interaction terms is one of the key limitations in the dipole-dipole interaction model, which leads to a significant underestimation of plasmon coupling at extremely small gaps. Additionally, the dipole model is essentially based on the electrostatic approximation which ignores any retardation effect. To properly describe the interaction at small gaps including the retardation effects would require the use of numerical modeling techniques such as FDTD and FEM. Before moving on, it is worth mentioning that the universal exponential dependence has led to the derivation of the so-called plasmonic ruler equation, which enables precise determination of distances in biological systems, opening many opportunities for biosensing [95].

Note that the previous discussion of dipole-dipole coupling focused only on the symmetric mode where the two individual dipoles are parallel to each other. As stated earlier, the anti-symmetric mode with anti-parallel dipoles has a small net dipole moment and thus interacts only weakly with light. This is not true when the anti-symmetric mode possesses a large magnetic moment. In this case, the anti-symmetric mode interacts strongly with light through its magnetic field. A dimer of small spherical nanoparticles does not support strong magnetic resonance but a pair of nanorods can. A pair of gold nanorods was shown to support a strong magnetic resonances [98,99] and soon after

Figure 8 Plasmon coupling in gold nanoparticle dimer. (a) Spectral position of the extinction maximum vs. interparticle distance for seven gold nanodisk pairs fabricated by electron-beam lithography (From [88]). **(b)** Calculated fractional plasmon peak shift vs the ratio of interparticle gap to nanodisk diameter, showing that the scaled data points for the different disc sizes follow a common trend, which can be fit together to the single-exponential decay (solid curves) $y = ae^{-x/\tau}$ with and $\tau = 0.23 \pm 0.03$ (From Ref. [95]).
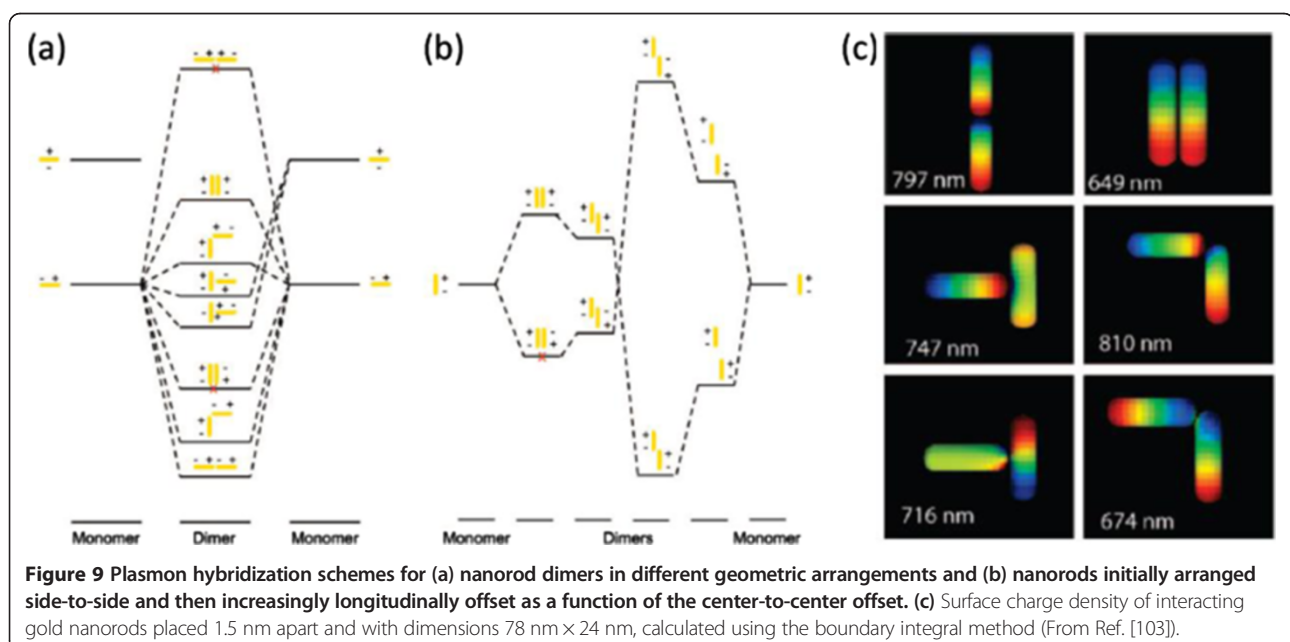
used to construct negative index material [100]. A similar behavior was also observed in a pair of nanoholes in two closely spaced metal films, which is expected to exhibit the same properties as the nanorod pair through the Babinet principle [101]. The nanohole pair design was then adapted to the fishnet structure which is known to be the most effective design for negative index [102]. Later, nanorod pairs with various different arrangements were investigated [103]. The hybridization scheme for various geometries is shown in Figure 9 together with the surface change densities for various plasmon modes. Here the hybridization scheme was obtained by the plasmon hybridization model and the surface charge density by the boundary integral method, both of which are described in Section 2.4. As shown in Figure 9(a), the single nanorod supports two resonances, longitudinal and transverse modes where the transverse mode has a higher energy due to the smaller transverse dimension. When the two nanorods are placed close together, the near-field interaction leads to hybridization and mode splitting where the symmetric and anti-symmetric combinations form bonding and anti-bonding modes. In the perfectly symmetric arrangements of end-to-end and side-to-side pairing, the anti-symmetric combination results in perfect cancellation of dipole moments. Thus the resultant hybridized mode is dark and does not respond to the incident light. Note that, unlike the nanorod pair used to observe magnetic resonance, which has one nanorod on top of the other so that the induced magnetic moment can align with the incident magnetic field, these nanorod pairs are all fabricated on the same plane and thus no magnetic interaction is expected. The energies of the hybridized modes are easily understood by the electrostatic interaction between electronic charge densities. For example, in the end-to-end pair, the anti-symmetric mode has the same charge concentrated near the gap, resulting in high energy while the symmetric mode has the opposite charge across the gap, leading to lower energy. Thus in this case, the symmetric mode becomes the bonding mode and the anti-symmetric mode forms the anti-bonding mode. For the side-to-side pair, the opposite is the case and the symmetric mode has higher energy than the anti-symmetric mode, making the anti-symmetric mode the bonding mode and the symmetric mode the anti-bonding mode. For other non-symmetric arrangements, the hybridized mode energy depends on the exact geometry. It should be noted that both the plasmon hybridization model and the boundary integral method used to generate Figure 9 take into account only the electrostatic interaction. The energy levels in Figure 9(a) and (b) are thus different from the experimentally measured plasmon peak positions, generally blue shifted from the experimental values due to the neglect of retardation effect.

2.3.2 Heptamers

To go beyond the simple dimer structure to more complex nanostructures, one needs a systematic way to classify various eigenmodes with complex symmetry properties. The group representation theory provides a power means to accomplish that [23]. For a given eigenvalue equation, $\mathbf{A}\mathbf{x}_n = a_n\mathbf{x}_n$, we can define a group of symmetry operators that leaves the operator $\mathbf{A}$ invariant. Note that the discussion here is generally applicable to any types of eigenvalue equations which could be the Schrödinger's equation in quantum mechanics, Maxwell's equation in optics and electromagnetics, or the fluid dynamics and surface charge

Figure 9 Plasmon hybridization schemes for (a) nanorod dimers in different geometric arrangements and (b) nanorods initially arranged side-to-side and then increasingly longitudinally offset as a function of the center-to-center offset. (c) Surface charge density of interacting gold nanorods placed 1.5 nm apart and with dimensions 78 nm × 24 nm, calculated using the boundary integral method (From Ref. [103]).

density equations used in the plasmon hybridization model and boundary integral formalism, respectively, discussed in Section 2.4. If a symmetry operator, **S**, leaves the operator **A** invariant, it is straightforward to show that the two operators commute with each other and share the same eigenstates. If all symmetry operators that leave the operator **A** invariant are found, then it is possible to classify all eigenstates of operator **A** in terms of how they transform under the various symmetry operators. In the language of group theory, all eigenstates of operator **A** can be indexed by the irreducible representations of the symmetry group. Now let us proceed to the plasmon modes in a trimer using the group representation theory. For a trimer composed of three identical nanoparticles placed at the corners of an equilateral triangle, the symmetry operators that leave the system invariant form the point group D_{3h} and thus the eigenmodes of a trimer can be classified by the irreducible representations of D_{3h}. For simplicity, we treat the plasmon mode of individual nanoparticle as a dipole mode, which is a good approximation for small particles. Then, the individual plasmon mode belongs to the $D^{(l=1)}$ irreducible representation of the full rotation group. For a trimer, we should consider the triple direct product of $D^{(l=1)}$ irreducible representations and their subsequent reduction into a combination of irreducible representations of point group D_{3h}, which yields [104],
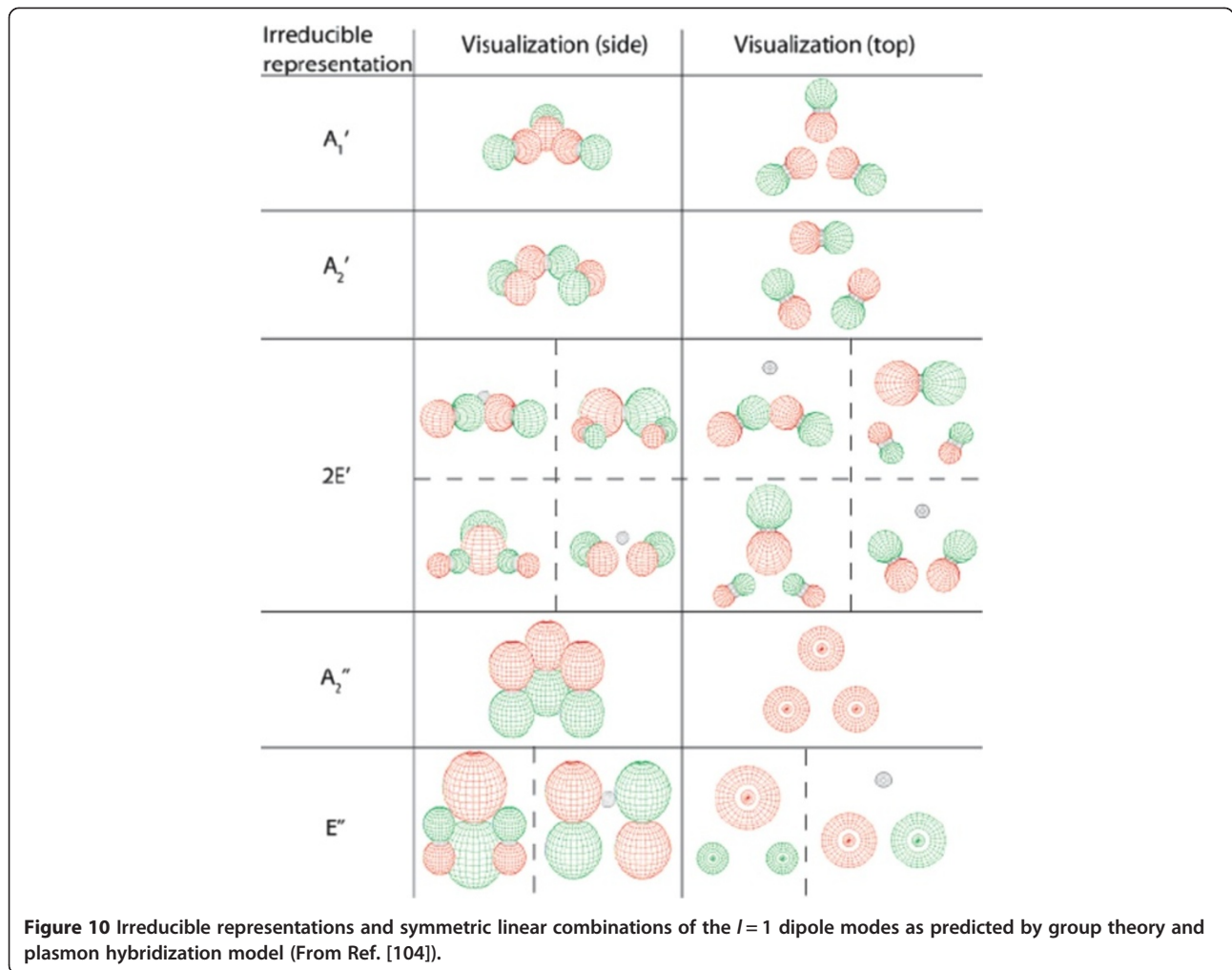
$$\Gamma_{trimer} = A_1' + A_2' + 2E' + A_2''E'' \qquad (40)$$

The transformation properties of the various irreducible representations of point group D_{3h} can be found in the character table available in the literature [23]. From the character table, one can then construct the projection operators and generate the symmetry-adapted basis functions, as shown in Figure 10, which transform according to the symmetry properties of the irreducible representations. The one-dimensional irreducible representations, A_1', A_2', A_1'', A_2'', have only one basis function each and the two-dimensional irreducible representations, E', E'', have two which are degenerate. Figure 10 is a powerful illustration of the symmetry properties of the hybridized plasmon modes. First, we notice the planar geometry of trimer naturally separates the in-plane and out-of-plane modes, which belong to the primed and double-primed irreducible representations, respectively. For light incident normally to the plane of the trimer, the out-of-plane modes are orthogonal to the incident electric field oscillation. Therefore, only the in-plane modes would interact with the incident light and the out-of-plane modes would not respond. Furthermore, the two in-plane modes, A_1', A_2', represent perfectly symmetric combinations of the individual dipoles resulting in zero

net dipole moment. These modes are therefore dark modes which do not interact with the incident light. The two in-plane E' modes possess net dipole moments and are the ones that will absorb or scatter light. It should be reminded that the actual plasmon modes excited by an incident light are dependent on the precise excitation conditions and would in general not be the E' modes shown in Figure 10. Rather, they may be expressed as a linear combination of the E' modes. A similar analysis has also been carried out for a nanorod trimer [17].

The group theory provides a powerful and effective way to describe more complex structures and extensive studies, both theoretical and experimental, have been conducted on quadrumers [56,104-106], pentamers [20,107], and hexamers [17,18,20]. The structure that received by far the most attention was the heptamer which is constructed by adding a central particle to a hexamer. The main reason for the interest has been the Fano resonance the heptamer supports. In most systems exhibiting resonance, the lineshape function describing the resonance is typically Lorentzian. However, when a discrete state interacts strongly with a continuum, a new resonance characterized by a distinctly asymmetric lineshape function may arise, as first discovered by Fano [108]. Since the origin of Fano resonance is the interference between the discrete and continuum quantum states, it is fundamentally a quantum phenomenon. However, the interference phenomenon is commonly observed in classical optics and Fano-like resonances have been observed in many systems. The oldest example is the Wood's anomaly arising from the interference between the tangentially diffracted wave and the incident wave [109]. It has also been observed in coupled waveguide-cavity systems, photonic crystals and plasmonic nanostructures for which many reviews are available [110-112]. In addition to the rich physics it reveals, Fano resonance also has many technological applications thanks to its high sensitivity to the environmental parameters [19]. Naturally, this led to the demonstration of optical sensing based on Fano resonances [113,114]. Here we review Fano resonances in heptamers in detail.

A heptamer is composed of seven nanoparticles in a geometry with 6-fold rotational symmetry. Six peripheral nanoparticles form a hexamer where the nanoparticles are placed at the corners of a regular hexagon. One central nanoparticle is located at the center of the hexagon. The heptamer has the same point group symmetry as hexamer, D_{6h}. Since the central nanoparticle is not connected to any other nanoparticles by the symmetry operators of point group D_{6h}, the irreducible representations for a heptamer can be found by the union of those for the hexamer formed by the peripheral nanoparticles and the central nanoparticle, $\Gamma_{hep} = \Gamma_{hex} + \Gamma_{cent}$. Similarly to the trimer case, considering only the dipole modes of
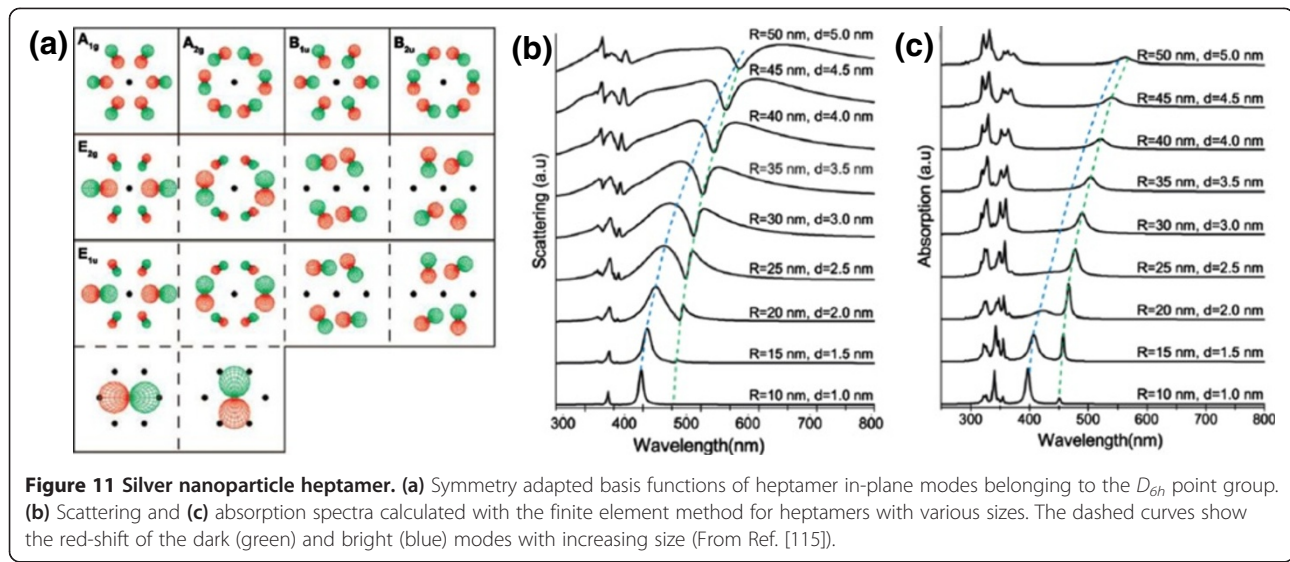
Figure 10 Irreducible representations and symmetric linear combinations of the $l = 1$ dipole modes as predicted by group theory and plasmon hybridization model (From Ref. [104]).

the individual nanoparticles, the irreducible representations of the hexamer, Γ_{hex}, are found by taking the direct product of six $l = 1$ irreducible representations, $\Gamma^{(l=1)}$, of the full rotation group and reducing it into the irreducible representations of the D_{6h} symmetry group. Likewise, the irreducible representation of the central nanoparticle is found by simply reducing $\Gamma^{(l=1)}$. The results are as follows

$$\Gamma_{hex} = A_{1g} + A_{2g} + B_{1u} + B_{2u} + 2E_{2g} + 2E_{1u}$$
$$\Gamma_{cent} = E_{1u} \qquad\qquad (40)$$
$$\Gamma_{hep} = A_{1g} + A_{2g} + B_{1u} + B_{2u} + 2E_{2g} + 3E_{1u}$$

where we only considered the in-plane modes in these reduction schemes. As explained earlier, the out-of-plane dipoles will not interact with the normally incident light. The symmetry-adapted basis functions for these irreducible representations are shown in Figure 11(a) [115]. Since the E irreducible representations are two-dimensional, they have two basis functions each. It is clearly seen that only the E_{1u} irreducible representation exhibits a net dipole moment and will thus interact with incident light. This
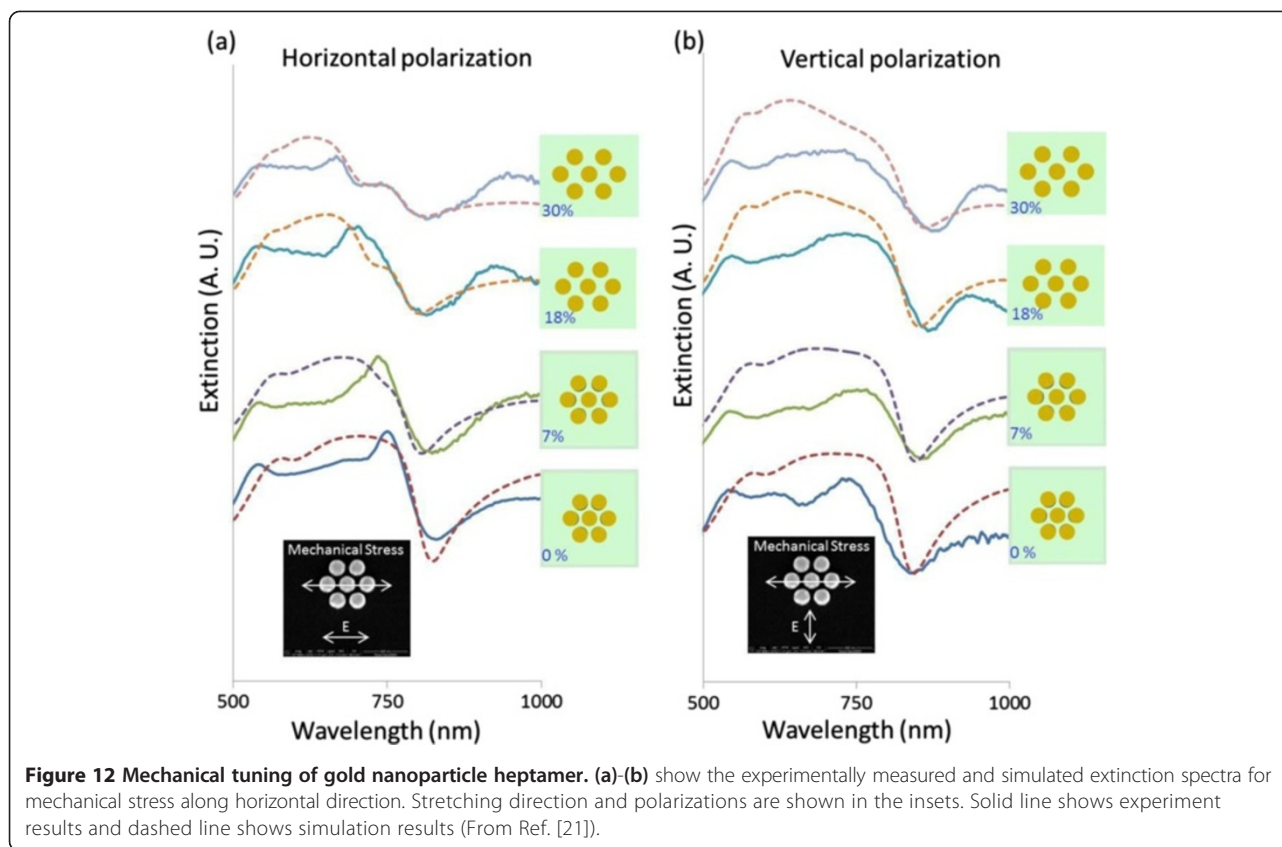
means all plasmon modes observed in experiments would belong to the E_{1u} mode and the mode profiles can be represented by linear combinations of the basis functions shown in Figure 11(a). To probe the plasmon modes in a heptamer, Mirin et al. calculated the absorption and scattering spectra of a silver nanoparticle heptamer with various sizes. As shown in Figure 11(b) and (c), in the smallest heptamer where the individual nanoparticles have a radius of 10 nm and are separated by 1 nm, three lowest energy peaks are observed in agreement with the plasmon hybridization model which predicts two bright modes at 340 nm and 380 nm and a dark mode at 450 nm. The bright modes are prominent in both the absorption and scattering spectra while the dark mode is weak and only visible in the absorption spectrum. Numerical simulations showed that the bright mode has a field profile indicating that the dipole moment of the central nanoparticle is aligned to that of the hexamer while the dark mode has the two dipoles anti-parallel, resulting in a small net dipole moment. As the particle sizes and gaps are increased proportionally, all modes exhibit red shifts due to the retardation

Figure 11 Silver nanoparticle heptamer. (a) Symmetry adapted basis functions of heptamer in-plane modes belonging to the D_{6h} point group. **(b)** Scattering and **(c)** absorption spectra calculated with the finite element method for heptamers with various sizes. The dashed curves show the red-shift of the dark (green) and bright (blue) modes with increasing size (From Ref. [115]).

effect and thus deviate from the results of plasmon hybridization which is valid only in the electrostatic regime. The retardation effect also broadens the peaks, particularly the bright modes, leading to a spectral overlap between the lowest bright mode and the dark mode. This results in the Fano resonance with its distinct asymmetric lineshape clearly visible in the scattering spectra for silver nanoparticle radii of 20 ∼ 40 nm. For radius of 50 nm, the energies of the bright and dark modes become almost the same. In the case, the Fano resonance presents itself as an antiresonance with a symmetric dip in the scattering spectrum.

The effect of symmetry lowering on the Fano resonance is of interest to both the fundamental physics and potential applications. Cui et al. fabricated gold heptamers on a flexible poly(dimethylsiloxane) (PDMS) membrane and applied mechanical stress while monitoring the evolution of the Fano resonance [21]. As shown in Figure 12, the Fano dip exhibited a blue shift with increasing mechanical stress for the polarization along the direction of stress while it shifted to lower frequencies for the perpendicular polarization. Also, for the parallel polarization, an additional Fano dip shows up at large mechanical strain values. Figure 12 also shows scattering spectra obtained by FEM simulations which agree very well with the experimental spectra. The same behavior was also confirmed by the generalized multiparticle Mie calculations following the theory described in Section 2.2. To gain insight into the observed behavior, the eigenmodes of the heptamer structure were obtained by solving the boundary integral eigenvalue equations for the charge distribution, as described in Section 2.4. Note that this technique is valid only in the static limit and thus the obtained plasmon energies are not the same as

the experimentally observed peak positions. Nevertheless, this study allows for the analysis of the eigenmodes with the group representation theory and thus correlate the symmetry of the system with that of the eigenmodes. As discussed earlier, the heptamer structure has the symmetry of point group D_{6h} and, among the irreducible representations of D_{6h}, E_{1u} is the only one with a net dipole moment and thus optically active. Furthermore, we only consider two lowest energy E_{1u} modes in the unstressed gold heptamer structure because all higher modes are masked by strong absorption by gold. In the first column of Figure 13, we show the charge distribution of the two lowest energy E_{1u} modes in an unstressed gold heptamer structure composed of seven identical gold spheres where the sphere diameter is 150 nm and gap between the spheres is 25 nm. Here the modes shown in Figure 13(a) and (b) belong to the lowest energy E_{1u} mode and (d) and (e) to the second lowest E_{1u} mode. The two-diomensional E_{1u} irreducible representation represetns a doubly degenerate mode with two orthogonal states having net dipole moment in the x and y directions, respectively. Accordingly, the four charge distributions shown in the first column of Figure 13 possess net dipole moment where (a) and (d) are x-dipoles and (b) and (e) are y-dipoles. Depending on the energy and the relative alignment of dipole moment of the center sphere to those of the six satellite spheres, the E_{1u} modes can be classified as dark or bright modes. The lower energy E_{1u} mode shown in Figure 13(a) and (b) is a dark mode where the dipole moment of center particle aligns against the dipole moments of satellite particles, making the total dipole moment small. On the other hand, the higher energy E_{1u} mode shown in Figure 13(d) and (e) is a bright mode where the dipole moments align

Figure 12 Mechanical tuning of gold nanoparticle heptamer. (a)-(b) show the experimentally measured and simulated extinction spectra for mechanical stress along horizontal direction. Stretching direction and polarizations are shown in the insets. Solid line shows experiment results and dashed line shows simulation results (From Ref. [21]).

together and add. The energies of these two E_{1u} modes were found to be 2.394 eV and 2.459 eV or 517.8 nm and 504.0 nm, respectively. These mode energy values would be accurate only for heptamers made of very small nanoparticles, as the boundary integral method is valid in the static limit only. For larger sizes, retardation effect will shift and broaden the modes. The resultant overlap and interference between the two modes lead to the Fano resonance. The bright mode will broaden much more significantly than the dark mode, resulting in Fano resonance which manifests itself in the form of a dip in the extinction spectrum as observed in Figure 12.

When the heptamer is subject to a uniaxial mechanical stress, the symmetry of the system is lowered to D_{2h}. The doubly degenerate E_{1u} mode splits into two nondegenerate modes belonging to B_{2u} and B_{3u} irreducible representations of the point group D_{2h}. Figure 13 shows the evolution of charge distribution as the mechanical stress is applied along the x direction. It clearly shows the original doubly degenerate modes split into x-dipole (B_{3u}) and y-dipole (B_{2u}) modes. Remarkably, the nature of the modes are preserved. That is, the bright E_{1u} mode splits into bright B_{2u} and B_{3u} modes while the dark E_{1u} mode spawns dark B_{2u} and B_{3u} modes. Also, all modes shift to shorter wavelengths with increasing mechanical strain values. However, the B_{3u} modes which have dipole

moment along the direction of mechanical stress shift more than the B_{2u} modes with dipole moment perpendicular to the mechanical stress. This leads to the distinct polarization dependence observed in Figure 12 as the B_{3u} modes interact with x-polarized light and B_{2u} with y-polarized light. Therefore, as the heptamer is stretched along the x direction, x-polairzed light would show resonance features at shorter wavelengths than the y-polarized light. Even when the retardation effects are included and the resonance peaks broaden and shift, this general behavior survives and leads to the experimental observation in Figure 12: the dip in the extinction spectrum due to the Fano resonance blue shifts for polarization parallel to the direction of mechanical stress but red shifts for polarization perpendicular to it. The exact numerical simulations by FEM and generalized multiparticle Mie theory also confirmed this.

In addition to the splitting of E_{1u} modes leading to the poalrization dependence, the scattering spectra for x polarization also show an additional dip at shorter wavelengths. The additional dip is apparent in the spectra for 30% and 45% strain for x polarization but is clearly missing in all spectra for y polarization. The origin of this second dip can be found by the group theoretical analysis. Briefly reiterating, in the unstressed heptamer structure possessing D_{6h} symmetry, only the E_{1u} modes
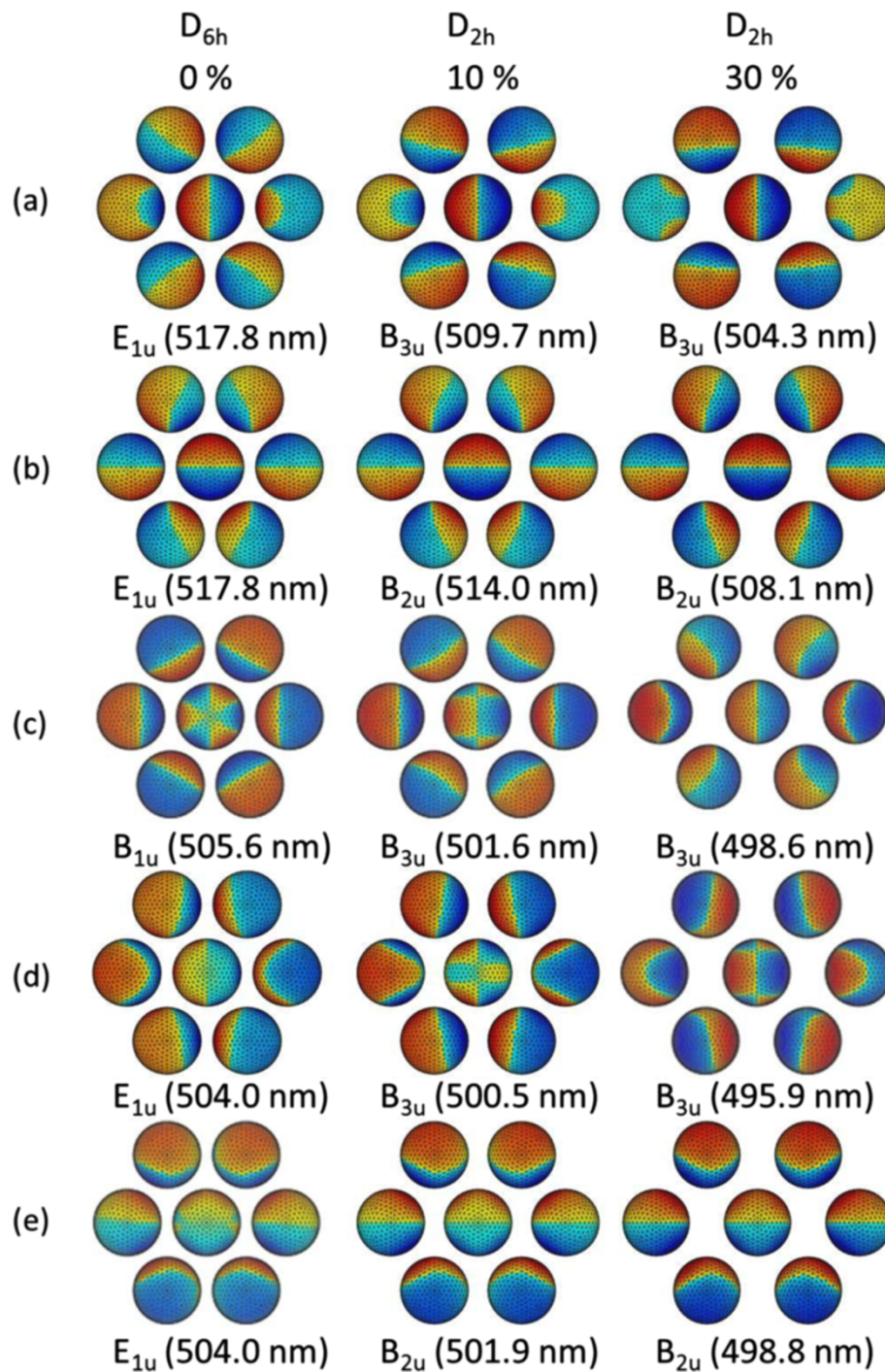
Figure 13 The evolution of charge distribution with uniaxial stress along the x direction. The first column shows the two lowest E_{1u} modes of unstressed heptamer and the B_{1u} mode. Second and third columns show B_{2u} and B_{3u} modes of the heptamer under 10% and 30% strains, respectively. The resonance wavelengths of the heptamers are also shown in paraenthesis (From Ref. [21]).

have non-zero dipole moments and thus are optically active. When the symmetry is lowered to D_{2h} by uniaxial stress, the E_{1u} modes split into B_{2u} and B_{3u} modes which interact with x- and y-polarized light, respectively. Since the unstressed heptamer has two E_{1u} modes in the

frequency range of interest, we obtain two B_{2u} and two B_{3u} modes, producing Fano resonance just as in the original unstressed heptamer. However, what is missing in this narrative is that the optically inactive B_{1u} mode in the unstressed heptamer becomes optically

active B_{3u} mode under uniaxial stress along the x direction. As shown in Figure 13(c), the charge distribution reveals that this B_{3u} mode is also a dark mode where the dipole moment of the center sphere aligns anti-parallel against those of the satelite spheres, thereby producing a second Fano dip in the scattering spectra. In constrast, there are no other modes of the unstressed heptamer evolving into B_{2u} mode within the frequency range we investigated and thus we do not see any additional dip for the y polarization.

Now we can take a step further and study which dipole components contribute to the formation of Fano resonance. For this, we consider nanorod heptamers composed of a circular center particle surrounded by six nanorods [22]. A circular nanoparticle supports a degenerate dipole mode with two orthogonal dipole moments having the same energy. The anisotropy of nanorod, however, lifts this degeneracy and the transverse mode has a substantially different energy than the longitudinal mode. This allows us to probe how the each dipole components hybridize separately. This design principle is schematically shown in Figure 14(a). The doubly degenerate dipole modes of the circular particle can be arranged into azimuthal dipoles and radial dipoles according to the six-fold rotational symmetry of the heptamer structure. We then replace the circular satellite particles with nanorods arranged azimuthally and radially. By designing the nanorod dimensions so that only the longitudinal modes are in the frequency range of interest, we can construct heptamers with only the azimuthal dipoles and radial dipoles. Subsequent numerical simulations revealed that the azimuthal nanorod heptamer exhibits a strong and well-defined Fano resonance (Figure 14(b)) but the radial nanorod heptamer does not support Fano resonance (Figure 14(c)). We then conducted a series of numerical simulations for a wide range of structural parameters to find that the azimuthal nanorod heptamers always support Fano resonance but the radial nanorod heptamers do not. These results indicate that the Fano resonance observed in circular heptamers are the result of hybridization of azimuthal dipole modes of the satellite particles with the center particle and that the radial dipole modes do not contribute.

The Fano resonance supported by the azimuthal nanorod heptamer was further investigated for their behavior under mechanical stress and symmetry lowering. As before, the mechanical stress was applied along the x (horizontal) direction. Figure 15 shows the simulated extinction and absorption spectra at the induced mechanical strain values of 0%, 13%, 26%, and 42%. For the polarization parallel to the mechanical stress (x direction), the Fano resonance exhibited a moderate blue shift while for the perpendicular polarization it showed a small blue shift. In addition to the spectral shifts with applied mechanical stress, the absorption spectra for the perpendicular polarization showed an additional feature at shorter wavelengths when the heptamer was under mechanical stress. This feature located near 620 nm was particularly noticeable at high strain values of 26% and 42%. The behavior of the spectral features in Figure 15 can be explained by analyzing the eigenmodes obtained by the boundary integral method. The evolution of charge distribution is dictated mainly by the symmetry reduction from D_{6h} to D_{2h} and is similar to that observed in the circular heptamer under mechanical stress described earlier. As was the case in the circular heptamer, the doubly degenerate E_{1u} mode of the azimuthal nanorod heptamer splits into two non-degenerate modes belonging to B_{2u} (y-dipole) and B_{3u} (x-dipole) irreducible representations of the point group D_{2h}. Furthermore, the bright E_{1u} mode was found to split into bright B_{2u} and B_{3u} modes and the dark E_{1u} mode into dark B_{2u} and B_{3u} modes. Both the dark and bright B_{2u} and B_{3u} modes shift to shorter
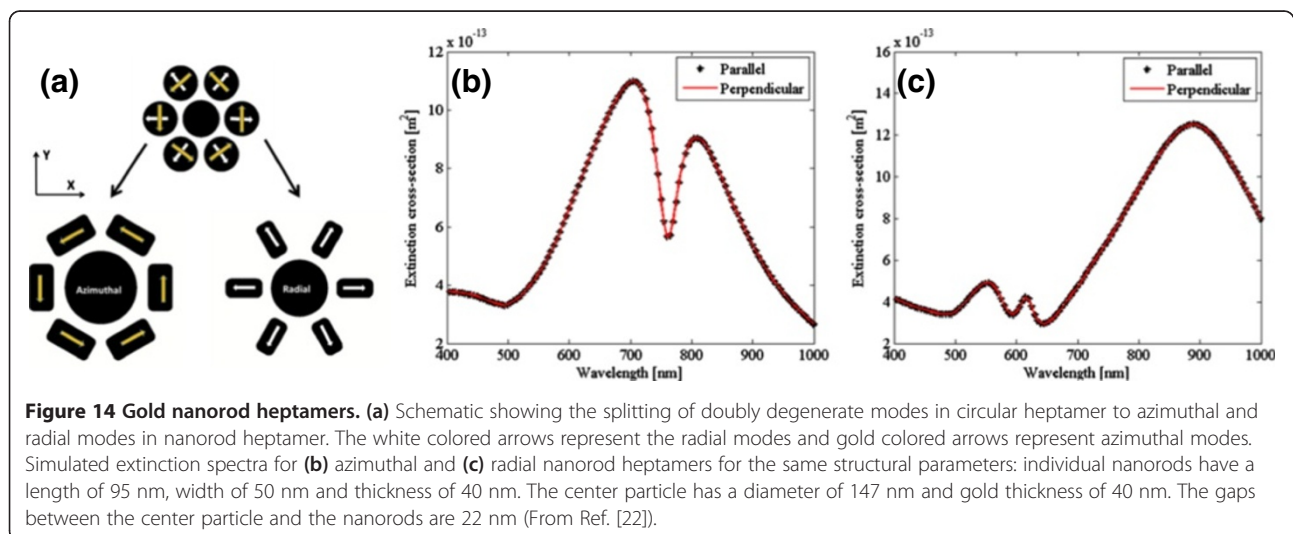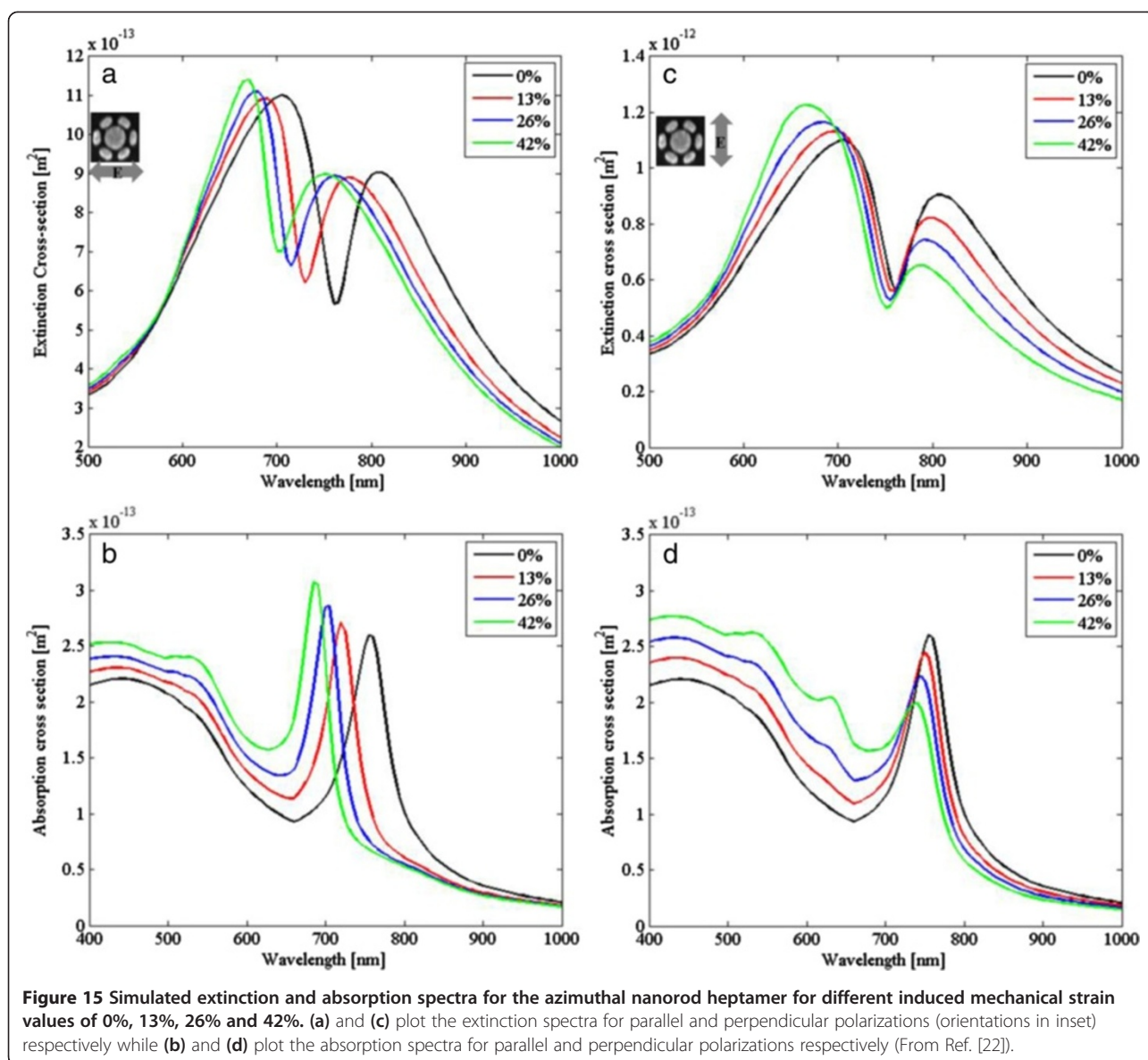

Figure 14 Gold nanorod heptamers. (a) Schematic showing the splitting of doubly degenerate modes in circular heptamer to azimuthal and radial modes in nanorod heptamer. The white colored arrows represent the radial modes and gold colored arrows represent azimuthal modes. Simulated extinction spectra for **(b)** azimuthal and **(c)** radial nanorod heptamers for the same structural parameters: individual nanorods have a length of 95 nm, width of 50 nm and thickness of 40 nm. The center particle has a diameter of 147 nm and gold thickness of 40 nm. The gaps between the center particle and the nanorods are 22 nm (From Ref. [22]).

Figure 15 Simulated extinction and absorption spectra for the azimuthal nanorod heptamer for different induced mechanical strain values of 0%, 13%, 26% and 42%. (a) and **(c)** plot the extinction spectra for parallel and perpendicular polarizations (orientations in inset) respectively while **(b)** and **(d)** plot the absorption spectra for parallel and perpendicular polarizations respectively (From Ref. [22]).

wavelengths with increasing mechanical strain values. However, the B_{3u} modes, which have dipole moment along the direction of mechanical stress, shifts more than the B_{2u} modes whose dipole moment is perpendicular to the mechanical stress, leading to the polarization dependence observed in the extinction and absorption spectra in Figure 15. Once again, the retardation effect results in overlap and interference between the dark and bright modes thus causing the Fano resonance to be observed as a dip in the extinction spectrum.

The additional absorption peak observed under stress can be explained by noting that the optically inactive B_{2u} mode in the unstressed heptamer becomes an optically active B_{2u} mode under uniaxial stress along the x direction. Here we have an unfortunate coincidence of having the same label for two very different modes. The B_{2u} irreducible

representation in D_{6h} symmetry has no net dipole moment and thus represents an optically inactive mode. However, the B_{2u} irreducible representation in D_{2h} symmetry has a finite dipole moment along the y-direction and thus represents an optically active mode that can interact with y-polarized light. The energy of this B_{2u} mode is higher than the lowest dark B_{2u} mode originating from the dark E_{1u} mode of unstressed heptamer, thereby producing an additional feature at a higher energy. The azimuthal nanorod heptamer differs from the circular heptamer in the behavior of this optically active mode. In the circular heptamer, the optically inactive B_{1u} mode was located between the two lowest energy E_{1u} modes in the unstressed heptamer and became optically active B_{3u} mode under uniaxial stress along the x direction. As a result, in the circular heptamer, the additional mode was observed

for x-polarized light. The difference between the circular heptamer and azimuthal nanorod heptamer is readily understood by comparing the eigenmode charge distributions. In the B_{1u} mode observed in the unstressed circular heptamer, the satellite particles have their dipole moments aligned along the radial direction (Figure 13c). In the azimuthal nanorod heptamer, this configuration would have had a much higher energy because the radial dimensions of the nanorods are much smaller than the circular particles used in circular heptamer. On the other hand, the B_{2u} mode in which the satellite particles have their dipole moments aligned along the azimuthal direction has a lower energy because the nanorods have larger dimensions along that direction. For these reasons, we find the B_{2u} mode is located between the two lowest energy E_{1u} modes in the azimuthal nanorod heptamer structure. These behaviors predicted by the theoretical modeling studies have been confirmed by experiments on gold nanorod heptamers fabricated by electron-beam lithography [22].

3 Conclusion and outlook

Plasmonics in mutually interacting nanostructures is an exciting field with rich physics and numerous potential applications. The recent progress clearly demonstrates that plasmonic nanostructures allow us to precisely control the nanoscale optical modes and how they interact with one another. These capabilities make the coupled plasmonic nanostructures an ideal platform to study nanoscale optical phenomena and build optical devices with novel functionalities. Though fundamentally a quantum mechanical entity, surface plasmons can be described well by classical electrodynamics in most cases. The theoretical framework presented in this review provides a firm foundation for designing interesting structures and analyzing their properties. Also, the strong field enhancement near the metal surface and the complex field profiles resulting from the interaction among the nanostructures makes the optical properties highly sensitive to the environment and consequently leads to exotic properties such as perfect absorption, invisibility and Fano resonance.

Some of the latest developments in the coupled plasmonic systems deal specifically with the quantum mechanical nature of the phenomenon. In surface enhanced Raman scattering and many other applications, it is generally advantageous to achieve high local field strength. In the simplest geometry of a dimer, a smaller gap supports higher field. However, when the two nanoparticles in a dimer are nearly touching, the electrons may tunnel through the gap, resulting in a dramatic decrease of local field strength and shift of plasmon energy [26,116]. Furthermore, at such a small length scale, the abrupt interface between two materials is unrealistic and the non-locality of the dielectric function has to be considered [117]. These considerations have led to the development

of a quantum-corrected model that could correctly reproduce the fully quantum mechanical calculations [118]. Unveiling the quantum mechanical nature of the gap plasmons in extremely small gaps remains an active research field with hopes of discovering new physics and also with potential for developing novel quantum devices.

Another interesting subject of fundamentally quantum nature is the coupling between plasmon and atomic or molecular exciton. The interaction between plasmon and exciton is of great fundamental interest with strong technological implications in organic electronics and photovoltaics. It has been shown that the surface plasmon can be used to control the relaxation pathways of molecular excitons [119]. Furthermore, in a fashion similar to plasmon hybridization, atomic or molecular exciton can hybridize with plasmon, forming a new quantum mechanically entity sometimes called plexciton [120,121]. The strong coupling between plasmon and exciton has recently been observed in an organic photovoltaic material [122]. The strong interaction could result in dramatic changes in excitation and relaxation dynamics of the molecular excitons, opening new opportunities in controlling and engineering the optical processes in organic materials.

In closing, surface plasmons provide a powerful means to gain access to the near field components that could result in a wide range of unconventional properties. Controlling and manipulating the mutual interactions among the plasmonic nanostructures offer design flexibility and engineering freedom unparalleled by any other photonics technologies. Obtaining high quality materials with low loss in precise nanoscale geometry will continue to be a challenge but the remarkable progress in nanofabrication technologies in the past decades makes it a perfect time to invest in research on the plasmonic nanostructures.

References
1. DK Gramotnev, SI Bozhevolnyi, plasmonics beyond the diffraction limit. Nat. Photon. **4**(2), 83–91 (2010)
2. J-S Lee, MS Han, CA Mirkin, Colorimetric Detection of Mercuric Ion (Hg2+) in Aqueous Media using DNA-Functionalized Gold Nanoparticles. Angew. Chem. **119**(22), 4171–4174 (2007)
3. JJ Storhoff, R Elghanian, RC Mucic, CA Mirkin, RL Letsinger, One-pot colorimetric differentiation of polynucleotides with single base imperfections using gold nanoparticle probes. J. Am. Chem. Soc. **120**(9), 1959–1964 (1998)
4. J Chen, F Saeki, BJ Wiley, H Cang, MJ Cobb, Z-Y Li, L Au, H Zhang, MB Kimmey, Li, Y Xia, Gold Nanocages: Bioconjugation and Their Potential Use as Optical Imaging Contrast Agents. Nano Lett. **5**(3), 473–477 (2005)
5. EB Dickerson, EC Dreaden, X Huang, IH El-Sayed, H Chu, S Pushpanketh, JF McDonald, MA El-Sayed, Gold nanorod assisted near-infrared plasmonic photothermal therapy (PPTT) of squamous cell carcinoma in mice. Cancer Lett. **269**(1), 57–66 (2008)
6. KY Lin, AF Bagley, AY Zhang, DL Karl, SS Yoon, SN Bhatia, Gold nanorod photothermal therapy in a genetically engineered mouse model of soft tissue sarcoma. Nano LIFE **1**(3), 277–287 (2010)
7. S Nie, SR Emory, Probing single molecules and single nanoparticles by surfaceenhanced Raman scattering. Science **275**(5303), 1102–1106 (1997)

8. AM Michaels, M Nirmal, LE Brus, Surface Enhanced Raman Spectroscopy of Individual Rhodamine 6G Molecules on Large Ag Nanocrystals. J. Am. Chem. Soc. **121**(43), 9932–9939 (1999)

9. JR Lakowicz, Radiative decay engineering 5: metal-enhanced fluorescence and plasmon emission. Anal. Biochem. **337**(2), 171–194 (2005)

10. P Andrew, Energy Transfer Across a Metal Film Mediated by Surface Plasmon Polaritons. Science **306**(5698), 1002–1005 (2004)

11. M Lunz, VA Gerard, YK Gun'ko, V Lesnyak, N Gaponik, AS Susha, AL Rogach, AL Bradley, Surface Plasmon Enhanced Energy Transfer between Donor and Acceptor CdTe Nanocrystal Quantum Dot Monolayers. Nano Lett. **11**(8), 3341–3345 (2011)

12. L Novotny, N van Hulst, Antennas for light. Nat. Photon. **5**(2), 83–90 (2011). 54

13. E Prodan, C Radloff, NJ Halas, P Nordlander, A hybridization model for the plasmon response of complex nanostructures. Science **302**(5644), 419–422 (2003)

14. P Nordlander, C Oubre, E Prodan, K Li, MI Stockman, Plasmon hybridization in nanoparticle dimers. Nano Lett. **4**(5), 899–903 (2004)

15. VK Lin, SL Teo, R Marty, A Arbouet, C Girard, E Alarcon-Llado, SH Liu, MY Han, S Tripathy, A Mlayah, Dual wavelength sensing based on interacting gold nanodisk trimers. Nanotechnology **21**(30), 305501 (2010)

16. AJ Mastroianni, SA Claridge, AP Alivisatos, Pyramidal and chiral groupings of gold nanocrystals assembled using DNA scaffolds. J. Am. Chem. Soc. **131**(24), 8455–8459 (2009)

17. DE Gómez, KC Vernon, TJ Davis, Symmetry effects on the optical coupling between plasmonic nanoparticles with applications to hierarchical structures. Phys. Rev. B **81**(7), 075414 (2010)

18. M Hentschel, M Saliba, R Vogelgesang, H Giessen, AP Alivisatos, N Liu, Transition from Isolated to Collective Modes in Plasmonic Oligomers. Nano Lett. **10**(7), 2721–2726 (2010)

19. JB Lassiter, H Sobhani, JA Fan, J Kundu, F Capasso, P Nordlander, NJ Halas, Fano Resonances in Plasmonic Nanoclusters: Geometrical and Chemical Tunability. Nano Lett. **10**(8), 3184–3189 (2010)

20. K Bao, NA Mirin, P Nordlander, Fano resonances in planar silver nanosphere clusters. Appl. Phys. A **100**(2), 333–339 (2010)

21. Y Cui, J Zhou, VA Tamma, W Park, Dynamic Tuning and Symmetry Lowering of Fano Resonance in Plasmonic Nanostructure. ACS Nano **6**(3), 2385–2393 (2012)

22. VA Tamma, Y Cui, J Zhou, W Park, Nanorod orientation dependence of tunable Fano resonance in plasmonic nanorod heptamers. Nanoscale **5**(4), 1592–1602 (2013)

23. M Tinkham, Group Theory and Quantum Mechanics (Dover Publications, Mineola, New York, 2003)

24. F Flores, F Garcia-Moliner, Model-independent theory of surface plasmons. Solid State Commun. **11**(9), 1295–1298 (1972)

25. G Barton, Some surface effects in the hydrodynamic model of metals. Rep. Prog. Phys. **42**(6), 963 (1979)

26. J Zuloaga, E Prodan, P Nordlander, Quantum Description of the Plasmon Resonances of a Nanoparticle Dimer. Nano Lett. **9**(2), 887–891 (2009)

27. Z Jacob, VM Shalaev, Plasmonics Goes Quantum. Science **334**(6055), 463–464 (2011)

28. DJ Bergman, MI Stockman, Surface plasmon amplification by stimulated emission of radiation: quantum generation of coherent surface plasmons in nanosystems. Phys. Rev. Lett. **90**(2), 027402 (2003)

29. A Archambault, F Marquier, J-J Greffet, C Arnold, Quantum theory of spontaneous and stimulated emission of surface plasmons. Phys. Rev. B **82**(3), 035411 (2010)

30. RH Ritchie, HB Eldridge, Optical emission from irradiated foils. I. Phys. Rev. **126**(6), 1935 (1962)

31. J Dionne, L Sweatlock, H Atwater, A Polman, Planar metal plasmon waveguides: frequency-dependent dispersion, propagation, localization, and loss beyond the free electron model. Phys. Rev. B **72**(7), 075405 (2005)

32. J Dionne, L Sweatlock, H Atwater, A Polman, Plasmon slot waveguides: Towards chip-scale propagation with subwavelength-scale localization. Phys. Rev. B **73**(3), 035407 (2006). 55

33. R Zia, M Selker, M Brongersma, Leaky and bound modes of surface plasmon waveguides. Phys. Rev. B **71**(16), 165431 (2005)

34. T Holmgaard, S Bozhevolnyi, Theoretical analysis of dielectric-loaded surface plasmonpolariton waveguides. Phys. Rev. B **75**(24), 245405 (2007)

35. G Mie, Beiträge zur Optik trüber Medien, speziell kolloidaler Metallösungen. Ann. Phys. **330**(3), 377–445 (1908)

36. YL Xu, Electromagnetic scattering by an aggregate of spheres. Appl. Opt. **34**(21), 4573–4588 (1995)

37. Y-L Xu, Electromagnetic scattering by an aggregate of spheres: far field. Appl. Opt. **36**(36), 9496–9508 (1997)

38. Y-L Xu, G BÅ, Comparison between multisphere light-scattering calculations: rigorous solution and discrete-dipole approximation. Astrophys. J. **513**(2), 894 (1999)

39. CF Bohren, DR Huffman, Absorption and Scattering of Light by Small Particles (JWILEY-VCH Verlag GmbH & Co. KGaA, Weinheim, 2008)

40. N Stefanou, V Karathanos, A Modinos, Scattering of electromagnetic waves by periodic structures. J. Phys. Condens. Matter **4**(36), 7389 (1992)

41. X Wang, XG Zhang, Q Yu, B Harmon, Multiple-scattering theory for electromagnetic waves. Phys. Rev. B **47**(8), 4161–4167 (1993)

42. A Moroz, Density-of-states calculations and multiple-scattering theory for photons. Phys. Rev. B **51**(4), 2068 (1995)

43. N Stefanou, A Modinos, Scattering of light from a two-dimensional array of spherical particles on a substrate. J. Phys. Condens. Matter **3**(41), 8135 (1991)

44. N Stefanou, V Yannopapas, A Modinos, Heterostructures of photonic crystals: frequency bands and transmission coefficients. Comput. Phys. Commun. **113**(1), 49–77 (1998)

45. JB Pendry, Photonic Band Structures. J. Mod. Opt. **41**(2), 209–229 (1994)

46. JCM Garnett, Colours in Metal Glasses and in Metallic Films. Philos. Trans. R. Soc. A Math. Phys. Eng. Sci. **203**(359), 385–420 (1904)

47. WT Doyle, Optical properties of a suspension of metal spheres. Phys. Rev. B **39**(14), 9852 (1989)

48. V Yannopapas, Negative refraction in random photonic alloys of polaritonic and plasmonic microspheres. Phys. Rev. B **75**(3), 035112 (2007)

49. VA Tamma, JH Lee, Q Wu, W Park, Visible frequency magnetic activity in silver nanocluster metamaterial. Appl. Opt. **49**(7), A11–A17 (2010)

50. CF Bohren, Applicability of effective-medium theories to problems of scattering and absorption by nonhomogeneous atmospheric particles. J. Atmos. Sci. **43**, 468–475 (1986)

51. S Yoo, Q-H Park, Effective permittivity for resonant plasmonic nanoparticle systems via dressed polarizability. Opt. Express **20**(15), 16480–16489 (2012)

52. TC Choy, Effective Medium Theory (Oxford University Press, New York, 1999)

53. P Berini, Plasmon-polariton waves guided by thin lossy metal films of finite width: Bound modes of symmetric structures. Phys. Rev. B **61**(15), 10484 (2000)

54. P Berini, Plasmon-polariton waves guided by thin lossy metal films of finite width: Bound modes of asymmetric structures. Phys. Rev. B **63**(12), 125417 (2001)

55. H Wang, DW Brandl, P Nordlander, NJ Halas, Plasmonic Nanostructures: Artificial Molecules. Acc. Chem. Res. **40**(1), 53–62 (2007)

56. JA Fan, K Bao, C Wu, J Bao, R Bardhan, NJ Halas, VN Manoharan, G Shvets, P Nordlander, F Capasso, Fano-like Interference in Self-Assembled Plasmonic Quadrumer 56 Clusters. Nano Lett. **10**(11), 4680–4685 (2010)

57. I Mayergoyz, D Fredkin, Z Zhang, Electrostatic (plasmon) resonances in nanoparticles. Phys. Rev. B **72**(15), 155412 (2005)

58. VM Shalaev, Optical negative-index metamaterials. Nat. Photon. **1**(1), 41–48 (2007)

59. W Park, J Kim, Negative-Index Materials: Optics by Design. MRS Bull. **33**(10), 907–914 (2008)

60. Z-P Yang, L Ci, JA Bur, S-Y Lin, PM Ajayan, Experimental Observation of an Extremely Dark Material Made By a Low-Density Nanotube Array. Nano Lett. **8**(2), 446–451 (2008)

61. N Landy, S Sajuyigbe, J Mock, D Smith, W Padilla, Perfect Metamaterial Absorber. Phys. Rev. Lett. **100**(20), 207402 (2008)

62. D Lu, E Rengnath, Y Cui, Z Wang, Y Ding, W Park, Interaction of two plasmon modes in the organic photovoltaic devices with patterned back-electrode. Appl. Phys. Lett. **102**(24), 241114 (2013)

63. V Kravets, F Schedin, A Grigorenko, Plasmonic blackbody: Almost complete absorption of light in nanostructured metallic coatings. Phys. Rev. B **78**(20), 205405 (2008)

64. JD Jackson, Classical Electrodynamics (Wiley, New York, 1998)

65. FJ García-Vidal, JM Pitarke, JB Pendry, Effective medium theory of the optical properties of aligned carbon nanotubes. Phys. Rev. Lett. **78**(22), 4289 (1997)

66. VG Kravets, S Neubeck, AN Grigorenko, AF Kravets, Plasmonic blackbody: Strong absorption of light by metal nanoparticles embedded in a dielectric matrix. Phys. Rev. B **81**(16), 165401 (2010)

67. EFC Driessen, MJA de Dood, The perfect absorber. Appl. Phys. Lett. **94**(17), 171109 (2009)

68. C Hägglund, SP Apell, B Kasemo, Maximized Optical Absorption in Ultrathin Films and Its Application to Plasmon-Based Two-Dimensional Photovoltaics. Nano Lett. **10**(8), 3135–3141 (2010)

69. C Hägglund, SP Apell, Resource efficient plasmon-based 2D-photovoltaics with reflective support. Opt. Express 18(103), 343–356 (2010)

70. C Hägglund, G Zeltzer, R Ruiz, I Thomann, H-B-R Lee, ML Brongersma, SF Bent, Self-Assembly Based Plasmonic Arrays Tuned by Atomic Layer Deposition for Extreme Visible Light Absorption. Nano Lett. 13(7), 3352–3357 (2013)

71. M Svedendahl, P Johansson, M Käll, Complete Light Annihilation in an Ultrathin Layer of Gold Nanoparticles. Nano Lett. 13(7), 3053–3058 (2013)

72. A Alù, N Engheta, Achieving transparency with plasmonic and metamaterial coatings. Phys. Rev. E. 72(1), 016623 (2005)

73. A Alù, N Engheta, Multifrequency Optical Invisibility Cloak with Layered Plasmonic Shells. Phys. Rev. Lett. 100(11), 113901 (2008)

74. A Alù, N Engheta, Cloaking a Sensor. Phys. Rev. Lett. 102(23), 233901 (2009)

75. A Alù, N Engheta, Cloaked Near-Field Scanning Optical Microscope Tip for Noninvasive Near-Field Imaging. Phys. Rev. Lett. 105(26), 263906 (2010)

76. F Bilotti, S Tricarico, F Pierini, L Vegni, Cloaking aperture-less near-field scanning optical microscopy tips. Opt. Lett. 36(2), 211–213 (2011)

77. S Tricarico, F Bilotti, L Vegni, Reduction of optical forces exerted on nanoparticles covered by scattering cancellation based plasmonic cloaks. Phys. Rev. B 82(4), 045109 (2010)

78. VA Tamma, Y Cui, W Park, Scattering reduction at near-infrared frequencies using plasmonic nanostructures. Opt. Express 21(1), 1041–1056 (2013). 57

79. DE Aspnes, Local-field effects and effective-medium theory: A microscopic perspective. Am. J. Phys. 50, 704 (1982)

80. S Mühlig, A Cunningham, J Dintinger, M Farhat, SB Hasan, T Scharf, T Bürgi, F Lederer, C Rockstuhl, A self-assembled three-dimensional cloak in the visible. Sci. Rep. 3, 2328 (2013)

81. KL Young, MB Ross, MG Blaber, M Rycenga, Using DNA to Design Plasmonic Metamaterials with Tunable Optical Properties. Adv. Mater. 26(4), 653–659 (2014)

82. SY Park, AKR Lytton-Jean, B Lee, S Weigand, GC Schatz, CA Mirkin, DNAprogrammable nanoparticle crystallization. Nature 451(7178), 553–556 (2008)

83. D Nykypanchuk, MM Maye, D van der Lelie, O Gang, DNA-guided crystallization of colloidal nanoparticles. Nature 451(7178), 549–552 (2008)

84. CE Talley, JB Jackson, C Oubre, NK Grady, CW Hollars, SM Lane, TR Huser, P Nordlander, NJ Halas, Surface-Enhanced Raman Scattering from Individual Au Nanoparticles and Nanoparticle Dimer Substrates. Nano Lett. 5(8), 1569–1574 (2005)

85. P Muhlschlegel, HJ Eisler, OJF Martin, B Hecht, DW Pohl, Resonant optical antennas. Science 308(5728), 1607–1609 (2005)

86. T Atay, J-H Song, AV Nurmikko, Strongly Interacting Plasmon Nanoparticle Pairs: From Dipole–Dipole Interaction to Conductively Coupled Regime. Nano Lett. 4(9), 1627–1631 (2004)

87. KH Su, QH Wei, X Zhang, JJ Mock, DR Smith, S Schultz, Interparticle Coupling Effects on Plasmon Resonances of Nanogold Particles. Nano Lett. 3(8), 1087–1090 (2003)

88. W Rechberger, A Hohenau, A Leitner, JR Krenn, B Lamprecht, FR Aussenegg, Optical properties of two interacting gold nanoparticles. Opt. Commun. 220(1), 137–141 (2003)

89. L Gunnarsson, T Rindzevicius, J Prikulis, B Kasemo, M Käll, S Zou, GC Schatz, Confined Plasmons in Nanofabricated Single Silver Particle Pairs: Experimental Observations of Strong Interparticle Interactions. J. Phys. Chem. B 109(3), 1079–1087 (2005)

90. P Biagioni, J-S Huang, B Hecht, Nanoantennas for visible and infrared radiation. Rep. Prog. Phys. 75(2), 024402 (2012)

91. A Taflove, SG Johnson, A Oskooi, Advances in FDTD Computational Electrodynamics (Artech House, Norwood, MA, 2013)

92. AC Polycarpou, Introduction to the Finite Element Method in Electromagnetics (Morgan & Claypool Publishers, 2006).

93. U Kreibig, M Vollmer, Optical Properties of Metal Clusters (Springer Verlag, Berlin, 2010)

94. M Gluodenis, CA Foss, The Effect of Mutual Orientation on the Spectra of Metal Nanoparticle Rod–Rod and Rod–Sphere Pairs. J. Phys. Chem. B 106(37), 9484–9489 (2002)

95. PK Jain, W Huang, MA El-Sayed, On the Universal Scaling Behavior of the Distance Decay of Plasmon Coupling in Metal Nanoparticle Pairs: A Plasmon Ruler Equation. Nano Lett. 7(7), 2080–2088 (2007)

96. PK Jain, MA El-Sayed, Universal Scaling of Plasmon Coupling in Metal Nanostructures: Extension from Particle Pairs to Nanoshells. Nano Lett. 7(9), 2854–2858 (2007)

97. PK Jain, MA El-Sayed, Surface Plasmon Coupling and Its Universal Size Scaling in Metal Nanostructures of Complex Geometry: Elongated Particle Pairs and Nanosphere 58 Trimers. J. Phys. Chem. C 112(13), 4954–4960 (2008)

98. VA Podolskiy, AK Sarychev, VM Shalaev, Plasmon modes in metal nanowires and left-handed materials. J. Nonlinear Optic. Phys. Mat. 11(1), 65–74 (2002)

99. VA Podolskiy, AK Sarychev, VM Shalaev, Plasmon modes and negative refraction in metal nanowire composites. Opt. Express 11(7), 735–745 (2003)

100. VM Shalaev, W Cai, UK Chettiar, HK Yuan, AK Sarychev, VP Drachev, AV Kildishev, Negative index of refraction in optical metamaterials. Opt. Lett. 30(24), 3356–3358 (2005)

101. S Zhang, W Fan, N Panoiu, K Malloy, R Osgood, S Brueck, Experimental Demonstration of Near-Infrared Negative-Index Metamaterials. Phys. Rev. Lett. 95(13), 137404 (2005)

102. G Dolling, C Enrich, M Wegener, CM Soukoulis, S Linden, Simultaneous negative phase and group velocity of light in a metamaterial. Science 312(5775), 892–894 (2006)

103. AM Funston, C Novo, TJ Davis, P Mulvaney, Plasmon Coupling of Gold Nanorods at Short Distances and in Different Geometries. Nano Lett. 9(4), 1651–1658 (2009)

104. DW Brandl, NA Mirin, P Nordlander, Plasmon Modes of Nanosphere Trimers and Quadrumers. J. Phys. Chem. B 110(25), 12302–12310 (2006)

105. Z Zhang, A Weber-Bargioni, SW Wu, S Dhuey, S Cabrini, PJ Schuck, Manipulating nanoscale light fields with the asymmetric bowtie nano-colorsorter. Nano Lett. 9(12), 4505–4509 (2009)

106. M Rahmani, T Tahmasebi, Y Lin, B Lukiyanchuk, TYF Liew, MH Hong, Influence of plasmon destructive interferences on optical properties of gold planar quadrumers. Nanotechnology 22(24), 245204 (2011)

107. SJ Barrow, X Wei, JS Baldauf, AM Funston, P Mulvaney, The surface plasmon modes of self-assembled gold nanocrystals. Nat. Commun. 3, 1275 (2012)

108. U. Fano, "On the absorption spectrum of noble gases at the arc spectrum limit," arXiv.org, vol. cond-mat.other. 08-Feb-2005 http://arxiv.org/abs/cond-mat/0502210.

109. A Hessel, AA Oliner, A new theory of Wood's anomalies on optical gratings. Appl. Opt. 4(10), 1275–1297 (1965)

110. B luk'yanchuk, NI Zheludev, SA Maier, NJ Halas, P Nordlander, H Giessen, CT Chong, The Fano resonance in plasmonic nanostructures and metamaterials. Nat. Mater. 9(9), 707–715 (2010)

111. A Miroshnichenko, S Flach, Y Kivshar, Fano resonances in nanoscale structures. Rev. Mod. Phys. 82(3), 2257–2298 (2010)

112. Y Francescato, V Giannini, SA Maier, Plasmonic Systems Unveiled by Fano Resonances. ACS Nano 6(2), 1830–1838 (2012)

113. N Liu, T Weiss, M Mesch, L Langguth, U Eigenthaler, M Hirscher, C Sönnichsen, H Giessen, Planar Metamaterial Analogue of Electromagnetically Induced Transparency for Plasmonic Sensing. Nano Lett. 10(4), 1103–1107 (2010)

114. C Wu, AB Khanikaev, R Adato, N Arju, AA Yanik, H Altug, G Shvets, Fanoresonant asymmetric metamaterials for ultrasensitive spectroscopy and identification of molecular monolayers. Nat. Mater. 11(1), 69–75 (2012)

115. NA Mirin, K Bao, P Nordlander, Fano Resonances in Plasmonic Nanoparticle Aggregates †. J. Phys. Chem. A 113(16), 4028–4034 (2009)

116. J Zuloaga, E Prodan, P Nordlander, Quantum Plasmonics: Optical Properties and Tunability of Metallic Nanorods. ACS Nano 4(9), 5269–5276 (2010)

117. FJ García de Abajo, Nonlocal Effects in the Plasmons of Strongly Interacting Nanoparticles, Dimers, and Waveguides. J. Phys. Chem. C 112(46), 17983–59–17987 (2008)

118. R Esteban, AG Borisov, P Nordlander, J Aizpurua, Bridging quantum and classical plasmonics with a quantum-corrected model. Nat. Commun. 3, 825 (2012)

119. G Wiederrecht, J Hall, A Bouhelier, Control of Molecular Energy Redistribution Pathways via Surface Plasmon Gating. Phys. Rev. Lett. 98(8), 083001 (2007)

120. NT Fofang, NK Grady, Z Fan, AO Govorov, NJ Halas, Plexciton Dynamics: Exciton–Plasmon Coupling in a J-Aggregate–Au Nanoshell Complex Provides a Mechanism for Nonlinearity. Nano Lett. 11(4), 1556–1560 (2011)

121. A Manjavacas, FG de Abajo, P Nordlander, Quantum plexcitonics: strongly interacting plasmons and excitons. Nano Lett. 11(6), 2318–2323 (2011)

122. N Azarova, AJ Ferguson J, van de Lagemaat, E Rengnath, W Park, JC Johnson, Coupling between a Molecular Charge-Transfer Exciton and Surface Plasmons in a Nanostructured Metal Grating, J. Phys. Chem. Lett. 2658–2663 (2013).